Bachelor Graduation Project Thesis

Portable Parameter Analyser for Organs-on-Chip Charge Sensor Model

Written By:
Maurice van der Maas
Kevin dos Reis Vezo

Delft University of Technology

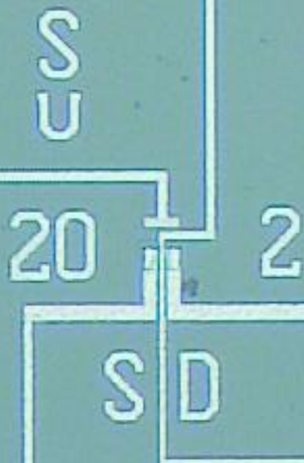

TU Delft Delft University of Technology

Challenge the future

Portable Parameter Analyser for Organs-on-Chip
Charge Sensor Model

Bachelor Graduation Project

Maurice van der Maas - 4446380
Kevin dos Reis Vezo - 4548086

Supervisors
Dr. Massimo Mastrangeli
Dr. Marco Spirito

Thesis committee
Prof. Dr. Peter Palensky
Dr. Massimo Mastrangeli
Dr. Marco Spirito
Hande Aydogmus
Carmine de Martino

Tuesday, 30th June, 2020
Version: 30th June, 2020

UNDER EMBARGO UNTIL 1st May, 2021

DELFT UNIVERSITY OF TECHNOLOGY

FACULTY OF ELECTRICAL ENGINEERING, MATHEMATICS AND COMPUTER SCIENCE

BSC ELECTRICAL ENGINEERING PROGRAMME

TU Delft Delft University of Technology

Challenge the future

Abstract

Real-time cell culture media monitoring can be conducted by Organ-on-Chip (OoC) ion-sensitive floating-gate field-effect transistor based sensors (ISFGFET). A method of modelling the sensor is described and implemented in the Advanced Design System (ADS) design and simulation software. The model is validated using measurement data of the sensor when exposed to an aqueous solution and in a 'dry' scenario. The model is utilized for an overall sensitivity analysis and the effect of the sensor dimensions on the sensitivity to charge variation that are immobilized on the sensing area surface. In addition to a SPICE compatible floating gate, level 3 MOSFET parameters are extracted, along with a sensing area model that links changes in the floating gate voltage to changes in the pH of the solution. Subsequently, a bias point is determined based on measurement data and limiting factors. Finally, the sensitivity of the ISFGFET is analysed. Our results characterize the effect that the sensing area dimensions, control gate capacitance and bias point have on the sensitivity.

Preface

Over the course of two months, we have gotten the opportunity to put our electrotechnical knowledge and skills to the test. To obtain the degree of Bachelor of Science, we and two other groups engaged in the design of a portable parameter analyzer for Organs-on-Chip.
Unfortunately, the creation of a physical demonstrator was not allowed under the COVID-19 restrictions. Consequently, all work had to be done from home whereas we would have loved to work with our colleagues in person.

We would like to express our gratitude towards our supervisors Dr. Marco Spirito and Dr. Massimo Mastrangeli, who proposed this project and provided us with advice and feedback, while still allowing us some freedom in the interpretation and completion of the task.
Secondly, great appreciation goes out to our daily advisors Hande Aydogmus and Carmine de Martino for being a reliable first point of contact when questions arose.
Furthermore, we are grateful to Dr. Ioan Lager for orchestrating the EE3L11 course to which we owe this opportunity.
Moreover, we thank our fellow project members Eray Albayrak, Maarten Mens, Jillis Noordhoek and Yme Wesseling for their collaboration and great team spirit.
At last, our families too deserve our gratitude for the continuous support during this project and our bachelor.

Maurice van der Maas and Kevin dos Reis Vezo
Delft, June 2020

Contents

Abstract **i**

Preface **iii**

1 Introduction **1**
1.1 Organ-on-Chip (OoC) systems . . . 1
1.1.1 Problem definition . . . 2
1.2 Ion-Sensitive Floating-Gate Field-Effect Transistors (ISFGFET's) . . . 2
1.3 Project goal . . . 3
1.4 Thesis structure . . . 3

2 Program of Requirements **5**

3 Sensor modelling **7**
3.1 ISFGFET analysis . . . 7
3.1.1 Operating principle . . . 8
3.1.2 Charge variation detection . . . 8
3.2 Floating Gate modelling . . . 9
3.3 MOSFET modelling . . . 11
3.4 Sensing area modelling . . . 11
3.4.1 Electric Double Layer (EDL) Theory . . . 12
3.4.2 EDL modelling . . . 15

4 Model Validation **17**
4.1 ISFGFET Modelling results . . . 17
4.2 FGFET Validation discussion . . . 18
4.3 Sensing area model validation . . . 19
4.3.1 Conceptual validation . . . 19
4.3.2 Full model validation . . . 20

5 Sensitivity Analysis **21**
5.1 Sensitivity factors . . . 21
5.2 Floating gate capacitance . . . 22
5.2.1 Optimizing the floating gate capacitance . . . 22
5.3 Sensing area parameters . . . 22
5.3.1 Dissociation constants . . . 23
5.3.2 Sensing area capacitance . . . 24
5.4 MOSFET parameters . . . 26
5.5 Limiting factors . . . 28
5.6 Bias point selection . . . 29
5.6.1 Fowler-Nordheim tunneling . . . 29
5.6.2 Hot electron injection . . . 30
5.7 Simulation results . . . 32

5.8 Sensitivity discussion 32

6 Conclusion **33**
6.1 Conclusion 33
6.2 Recommendations 33

Bibliography **35**

Appendices **39**

A Collaboration **39**

B Derivations **41**
B.1 Compact modelling procedures 41
B.1.1 The transconductance, k 41
B.1.2 The threshold voltage, V_{T0} 42
B.1.3 channel-length modulation, λ 42
B.1.4 The saturation voltage, V_{DSAT} 42
B.1.5 LEVEL 3 extraction methods 42

C ADS **43**
C.1 FGFET parameter extraction schematic 43
C.2 ISFGFET with sensing area model 44

D MATLAB simulation **47**
D.1 EDL 47
D.2 Fowler-Nordheim tunneling estimation 49

Chapter 1

Introduction

1.1 Organ-on-Chip (OoC) systems

Problems in drug development and personalized disease treatments are the main impulse for the development of OoCs [1], which stem from a synthesis of tissue engineering and microfluidic technology. Now that dynamic fluid flow, electro-mechanical stimuli and controlled biochemistry can be purposed to provide a physiologically representative micro-environment to cell cultures, biomedical researchers can get a deeper understanding of the mechanisms and etiology behind the diseases. Various industries opt for human models to minimize toxicological risks where physiological relevancy can increase the certainty required under the increasingly strict regulations. Besides, conventional methods nowadays still include animal testing despite being subject to ethical questioning. In the coming years the remaining technological challenges for OoC systems will be tackled hopefully resulting in the key unmet needs being met.
At the Electronic Components, Technology and Materials (ECTM) group at TU Delft an OoC sensor has been developed and the design is now at a stage where a system can be developed to take the sensor out of the initial research environment, into a complete product that incorporates the sensor. The sensor in question consists of eight Floating Gate Field Effect Transistors (FGFET) designed to measure the changes in electrochemical charges in a (bio)chemical solution. As can be seen in Figure 1.1 the floating gates of the FGFETs extend into the sensing area, such that charges accumulated on the gates will modulate the gate-source voltage and therefore change the FGFET threshold voltage and drain current [2].

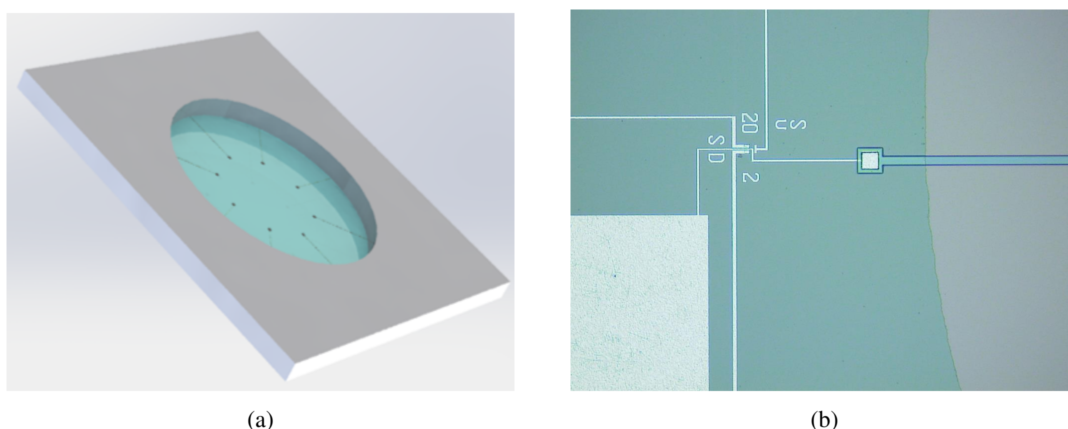

(a) (b)

Figure 1.1: a) Model of the sensor showing the 8 floating gates extending into the sensing area. b) Close-up made during the fabrication process, showing one of the transistors with the first polyimide insulation layer for the floating gate extending to the right of the figure [2].

1.1.1 Problem definition

Real-time cell culture condition monitoring is generally done in biological or clinical research environments that in contrast to engineering laboratories, are not equipped with sophisticated electrical measuring equipment. At this stage the end-user has not been given enough thought. Purchasing peripheral equipment with redundant functionality or complexity isn't cost-effective. Moreover source measure units (SMU) aren't necessarily easy to maintain and operate without extensive training. Furthermore, parameter analyzers take up too much space to fit inside an incubator. Thus a OoC specific portable parameter analyzer is desired. The OoC sensor should measure electrochemical changes on or in close proximity of the sensing area. The OoC sensor itself is already designed, however it needs to be modelled in order to characterize it and to see where it could be improved in order to increase the sensitivity. For the very small currents and voltages that need to be measured, the Electronic Circuits and Architectures (ELCA) group at the TU Delft already designed an instrumental amplifier which is given to the group. This design is evaluated together with the rest of the system in order to verify whether it can measure the small changes on the sensor. Three subgroups consisting of two students each were assigned to this project and were each given one of the following tasks:

1. The analysis of the power budget and heat exchange together with an interface design [3]
2. The calibration together with the design of a user-friendly GUI [4]
3. The modeling of the sensor and providing a sensitivity analysis

The third task will be the subject of this thesis and will be discussed in more detail in Section 1.3. First, more background will be given in the next section (1.2).

1.2 Ion-Sensitive Floating-Gate Field-Effect Transistors (ISFGFET's)

Transistor based sensors are promising as implementation for (bio)chemical sensors, mainly due to their small dimensions, low power consumption and on-chip amplification ability. Initially, implementations of ion-sensitive solid-state devices for the detection of ion activities in electrochemical and biological environments were centered around Ion-Sensitive Field-Effect Transistors (ISFET's). The first implementation of an ISFET was described in 1970 by Bergveld [5]. Generally, in a field-effect transistor, gate metal is used to apply a gate potential, which would induce a conducting channel in the silicon between source and drain. The silicon dioxide layer, on top of an Ion-Sensitive FET (ISFET), however, has no gate metal and is directly exposed to an aqueous solution (Figure 1.2). The oxide exposed to ion concentrations in the solution forms a double layer over its surface which affects the channel conductance. As a result, the ISFET is sensitive to changes in the pH [5, 6]. This sensitivity can be seen in a modulation of the threshold voltage, while a reference electrode functions as the actual gate metal [7]. Although ISFET's themselves can be miniaturized and are compatible with integrated circuits, external reference electrodes, cannot be miniaturized [8]. This disadvantage limits the potential of ISFET's for the use in OoC systems. Floating-Gate ISFET's (ISFGFET's) or Charge-Modulated FET's (CMFET's) provide a solution to this problem. [9].

An ISFGFET consists of a field-effect transistor, where the gate is isolated from the rest of the device. The gate voltage is controlled via a control gate, which is capacitively coupled to the floating gate (Figure 1.2) and effectively replaces the reference electrode used in conjunction with ISFET's. The operating principle of the ISFGFET is centered around the principle of charge conservation. Due to the floating gate being isolated, the total charge in the floating gate must remain constant. The total amount of charge contributing to the overall floating gate voltage, however *can*, in fact, change. Variations here are possible due to charge redistribution in or from the section of the floating gate that is exposed, directly or through a spacing layer, to an aqueous solution. This charge redistribution is caused by either surface charge variation or directly by ionic charge variations in close proximity of the sensing area.
In the case of surface charge, ions or other charged particles like DNA strands can immobilize on the sensing surface, either covalently linked to a spacing layer between floating gate and solution, or directly to the

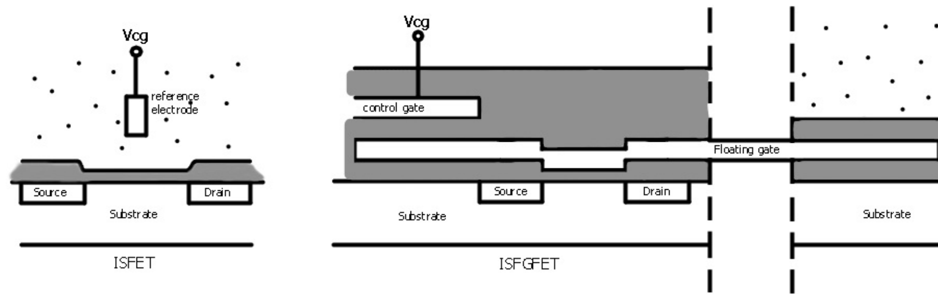

Figure 1.2: Left-hand side: ISFET cross-section, right-hand side: ISFGFET cross-section

floating gate area, in case no spacing layer is applied. Implementations of this concept have been developed for various sensing purposes, including DNA detection and hybridization [9–11], and the detection of other (bio)chemical molecules [12–14]. Even if charges do not link to the sensing surface, variation in ion concentrations in close proximity of the the sensing area surface can still cause redistribution of charge in the floating gate [15]. In this document, two different implementations of an ISFGFET will be studied. The sensor that is considered has a Ti gate that extends over a PDMS membrane. In the first implementation, the Ti gate is exposed to the solution at the sensing area. This sensing area has been exposed to air and has therefore a thin oxide layer on top. In the second implementation a silicon dioxide layer has been placed on top of the sensing areas. Both implementations allow for covalent bonding of ions to the sensing surface. We will therefore focus on the implementation where immobilized surface charge on the sensing area surface causes charge redistribution withing the floating gate.

1.3 Project goal

The goal of the application part of the project is firstly to derive a model of the already existing ISFGFET. This model must be able to perform DC sweeps for characterising the drain current as a function of sensing charge redistribution as well as time-domain analysis of the sensor drain current. A sensitivity analysis is performed using the derived model with the goal of finding the optimal operation point of the sensor and the ideal sensor dimensions in order to optimize the overall sensitivity to charge variation on or in the vicinity of the device sensing area. An additional goal is expansion of the sensing area model. The sensing area dynamics are initially simulated simply as variations in gate charge. This model can be expanded by incorporating the electric double layer on the surface of the sensing area in the solution into the model. This provides the ability to link variation in the drain current directly to variations in the pH of the solution [16]. This is important because it can be used to calibrate the sensor by comparing the drain current of the dry sensor to that of the sensor when exposed to a known solution.

1.4 Thesis structure

The structure of the thesis is as follows: Chapter 2 will go through the requirements for the sensor model, Chapter 3 goes through the design steps for the ISFGFET model, Chapter 4 will go through the validation steps and Chapter 5 will give a sensitivity analysis. Finally, Chapter 6 provides a conclusion suggestions for future work.

Chapter 2

Program of Requirements

Listed below are the requirements of the total system, from which the ones that are specifically targeted at the charge sensor model are highlighted in bold. A distinction is made between critical and optimizable requirements.

Mandatory system requirements:

- Must operate within an incubator at 37°C
- Must be resistant to the humidity of the incubator (IP59)
- Must be able to fit inside all microbiological incubators
- Battery-life must last at least 6 days
- Must be able to sense ion activity at the sensing interface by by means of ISFGFET drain current readout.
- Must be capable of real-time data read-out
- **Must visualize the drain current (I_D) characteristics**
- Must provide a comprehensible GUI for the end user
- Must have a calibration procedure for the sensor operating point and sensitivity

System trade-off requirements:

- Minimize power consumption
- Minimize heat dissipation
- **Maximize current and voltage resolution**
- Minimize volume
- **Maximize sensitivity by means of ISFGFET geometry optimization** and noise minimization

Model requirements: The model

- Must represent the implementation of the ISFGFET as described by [2].
- Must be able to simulate charge variation on or in close proximity of the sensing interface.
- Maximum deviation must not exceed more than 10% from the measurement data
- Must be able to simulate variations in sensing areas surface charge of at least 0.3 pC.
- Must be able to simulate changes in pH with an 10% accuracy from the measurement data.
- Must be compatible with the amplifier simulation environment (Advanced Design Systems).
- Dimensions must be easily scalable for validation purposes.

Chapter 3

Sensor modelling

In this chapter, the functionality of the sensor is described and a SPICE-compatible model is discussed. Section 3.1 discusses the operating principle of the ISFGFET and sets up some equations used for modelling the device. Section 3.2 describes a SPICE-compatible model for simulating the ISFGFET and sets up equations for the relevant parameters such as the control gate capacitance and parasitic capacitances. Section 3.3 discusses the MOSFET modelling and Section 3.4 describes a model for the sensing area to solution interface.

3.1 ISFGFET analysis

The ISFGFET that is used for the portable OoC analyser is shown in figure 3.1 along with its equivalent circuit. The transistor is fabricated on a silicon wafer, after which it is coated with a layer of PDMS [2]. Silicon is etched from the backside of the device, exposing the floating gate sensing area and the PDMS, which functions as a membrane on which cells are cultured. The floating gate consists of two parts. The aluminum part forms a parallel plate capacitor with the control gate. From the floating gate, a Ti extension, sandwiched between two polyimide layers, stretches over the PDMS membrane. The sensing area is formed by exposing part of the Ti extension (via a thin silicon dioxide spacing layer or directly) to the solution-under-test.

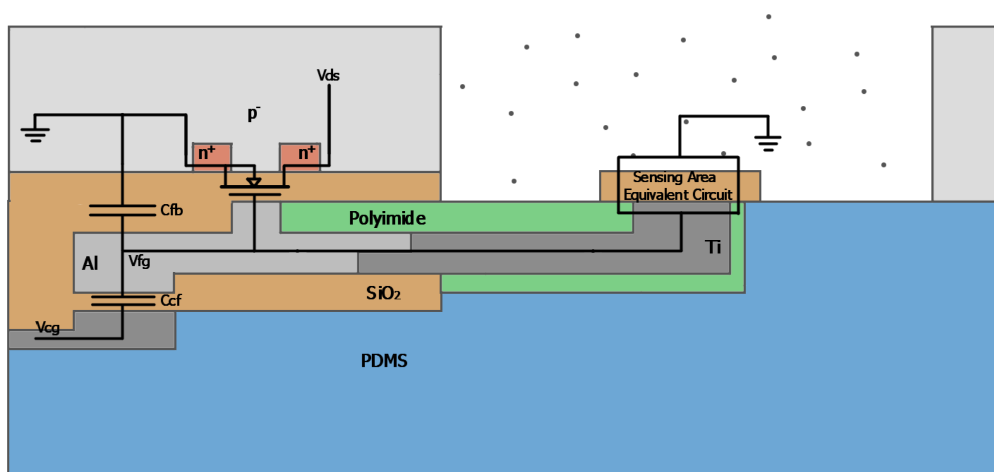

Figure 3.1: Cross section of the ISFGFET sensor and its equivalent circuit. Note that the silicon dioxide over the Ti is not necessarily added, depending on the application

3.1.1 Operating principle

Table 3.1: Description and units of the ISFGFET parameters

Parameter	Description	Unit
C_{CF}	control gate capacitance	F
C_{FB}	floating gate to substrate capacity	F
C_{SG}	total floating gate capacitance	F
V_{T0}	zero bias threshold voltage	V
V_{CG}	control gate voltage	V
V_{FG}	floating gate voltage	V
V_{THF}	effective ISFGFET threshold voltage	V
I_{D0}	drain current at bias point	A
g_m	MOSFET saturation region transconductance	A/V
Q_s	sensing area surface charge	C
Q_{F0}	trapped electric charge in the floating gate	C

As mentioned in section 1.2, variation in surface charges on the sensing area or charge density variations in the vicinity of the sensing area cause a redistribution of charge in the floating gate. This charge redistribution can be modelled as alterations in the effective floating gate charge, which is the charge that contributes to the floating gate voltage. A general model for CMFET's was described by Barbaro [9]. The floating gate voltage of such a device can be written as:

$$V_{FG} = \frac{C_{CF}}{C_{CF} + C_{FB}} V_{CG} + \frac{Q_{F0} - Q_i(Q_s)}{C_{CF} + C_{FB}} \tag{3.1}$$

Here, Q_{F0} is the initial charge on the floating gate, Q_s is the surface charge and Q_i it the charge that is induced directly below the sensing area. If the oxide thickness between the solution and the floating gate (t_{oxSA}) is much smaller than other dimensions, we can assume perfect induction which means that the magnitude of Q_i is equal to that of Q_s but opposite in sign, that is $Q_i = -Q_s$. In Section 3.4 we will look closer at how Q_i varies with Q_s.

The change in floating gate voltage is often modelled as a change in effective threshold voltage, which is the threshold voltage as seen from the control gate. However, effective charge variations are detected by variation in the measured drain current. As described in Chapter 5.6, it is recommended to operate the MOSFET in the saturation region. It is therefore more useful to look at the change in floating gate voltage due to effective charge variations directly. The expression for the floating gate voltage variation is as follows:

$$\Delta V_{FG} = \frac{\Delta Q_s}{C_{CF} + C_{FB}} \tag{3.2}$$

Note that the capacitance of the floating gate to the measured solution C_{SG} does not seem to affect the floating gate voltage or the change in floating gate here given a certain charge redistribution. This does not mean this capacitance is not an important factor. In section 3.4 we will see that C_{SG} influences the fraction of the immobilized surface charge that is reflected as effective charge redistribution in the floating gate and that the assumption of perfect induction is therefore not entirely valid.

3.1.2 Charge variation detection

To minimize variations in drain current due to the applied drain-source voltage, the MOSFET is operated in the saturation region. The goal is to derive an expression of the measured drain current as a function of the redistributed gate charge Q_s and the control gate voltage V_{CG}. To achieve this, we need to substitute equation 3.1 into the expression of the MOSFET transconductance. This is shown in Equation 3.3.

$$g_m = \frac{2I_D}{V_{FG} - V_{T0}} = \frac{2I_D(C_{CF} + C_{FB})}{C_{CF}V_{CG} + Q_{F0} + Q_s - V_{T0}(C_{CF} + C_{FB})} \tag{3.3}$$

Let us examine the drain current response to small variations of the sensing area surface charge. We assume that the contribution of the control gate voltage to the floating gate voltage is sufficiently larger than the contribution of the floating gate sensing area surface charge, that is: $C_{CF}V_{CG} \gg Q_{F0} + Q_s$. This is necessary in order to ensure that the magnitude of the drain current is much larger than the change in the drain current due to small charge variations at the sensing interface. The expression for the MOSFET transconductance as a function of the surface charge now simplifies to Equation 3.4. Changes in drain current due to very small changes in sensing area surface charge can now be expressed as a product of the transconductance and the change in floating gate voltage due to the change in surface charge.

$$g_m \simeq \frac{2I_D(C_{CF} + C_{FB})}{C_{CF}V_{CG} - V_{T0}(C_{CF} + C_{FB})} \tag{3.4}$$

$$\Delta I_D = g_m \Delta V_{FG} = g_m \frac{\Delta Q_s}{(C_{CF} + C_{FB})} = \frac{2I_{D0}\Delta Q_s}{C_{CF}V_{CG} - V_{T0}(C_{CF} + C_{FB})} \tag{3.5}$$

Where I_{D0} is the biased drain current and $I_{D0} \gg \Delta I_D$. The above equation shows that an increase in positive surface charge causes an increase in drain current for n-channel MOSFET's and a decrease for p-channel MOSFET's.

Using this approach, small changes of effective charge on the floating gate can be approximated. However, a more detailed model is necessary for characterizing the sensor behaviour for any bias point. We choose to implement this model in Advanced Design System (ADS), but the model concept can be used in any SPICE-based software.

3.2 Floating Gate modelling

Modelling the floating gate of a MOSFET accurately is a challenge in itself. Standard SPICE simulators are unable to process floating nodes, as they are unable to converge to a DC solution. This is because all nodes need a DC path to ground for SPICE to determine a DC voltage. Apart from DC convergence, the model must also be able to simulate alterations in the total gate charge, since charge redistribution due to surface charges on the sensing area can be modelled as charge alterations in the floating gate. An effective way of simplifying this problem is by splitting the floating gate into two nodes, as proposed by Rapp [17]. This concept is shown in figure 3.2.

An initial charge can be applied using the voltage source V_{init}. This voltage is equal to Q_{F0}/C_{tot}, where C_{tot} is the sum of C_{CF} and C_{FB}. The floating gate is connected to ground through the voltage source in series with a very large resistor, defined as R_{Huge}. This enables DC convergence, while in AC the node appears to be floating. The voltage from the FG node is projected to the actual floating gate (Figure 3.2 left circuit) using a voltage-controlled voltage source. The other terms contributing to the floating gate voltage are determined by the control voltage, the control gate capacitance and any floating gate parasitic capacitance and their corresponding voltages. Assuming the device substrate is held at ground potential, the sum term can be written as follows:

$$\sum \alpha_i V_i = \frac{C_{CG}}{C_{tot}} V_{CG} \tag{3.6}$$

Where C_{CG} is the control gate capacitance and V_{CG} is the control gate voltage. For this model, the sum term only consist of one term, because the sensing area oxide capacitance is not yet included in the model. In Section 3.4, the sum term is expanded to include the sensing area model.

As discussed earlier, the charge redistribution in the floating gate due to surface charge or charge concentrations in the direct vicinity of the sensing area can be modelled as alterations in floating gate effective charge and consequently a change in floating gate voltage. It is therefore possible to add the effective charge contribution factor to the initial floating gate voltage V_{init}. This allows for performing DC sweeps

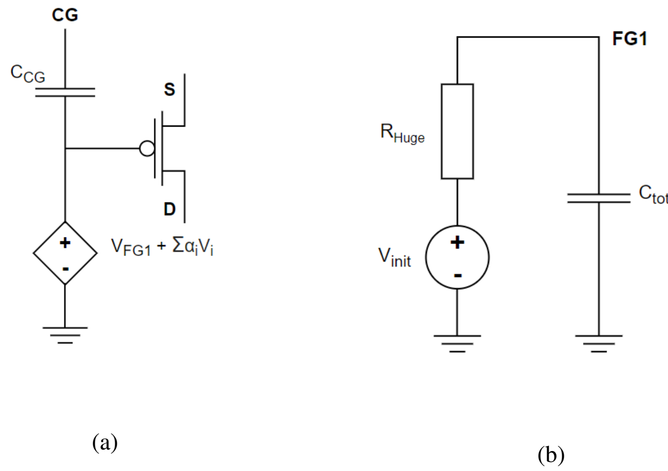

(a) (b)

Figure 3.2: (a) Model of a floating gate MOSFET. (b) A second node (FG1) is used to compute the charge on the floating node [17]. The computed potential at node FG1 is added to gate of the MOSFET in (a) using a voltage controlled voltage source.

to characterize the sensor behaviour at different amounts of surface charge. It is however not suitable for AC simulations since the the voltage source V_{init} is invisible to the floating gate in AC. For AC simulation, a current source is needed for transporting charge to and from the floating gate effective charge computation node. The resulting circuit is shown in figure 3.3.

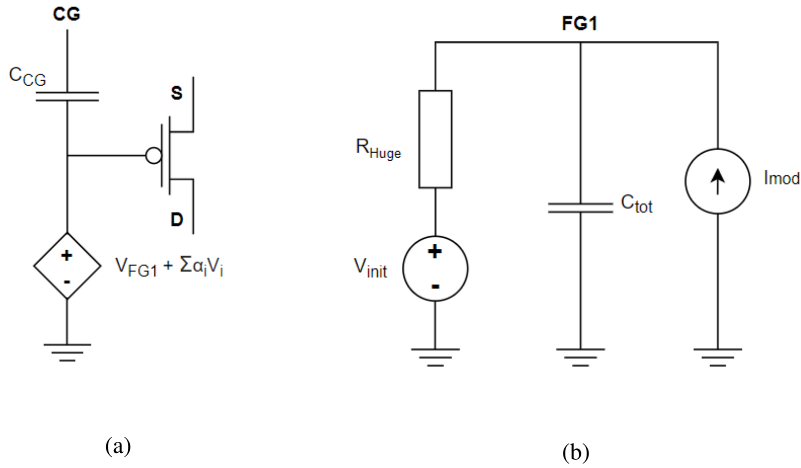

(a) (b)

Figure 3.3: (a) Model of a floating gate MOSFET. (b) A second node (FG1) is used again to compute the charge on the floating node. Charge can be added or removed from the node with the current source. The computed potential at node FG1 is added to gate of the MOSFET in (a) using a voltage controlled voltage source. (Compare with Figure 3.2)

The current I_{mod} here represents the charge redistribution through floating gate and is the derivative of a time-dependent surface charge induction function.

$$I_{mod} = -\frac{d}{dt}Q_i(t) = \frac{d}{dt}Q_s(t) \tag{3.7}$$

Modelling a change in surface charge in now fairly straightforward. Using Equation 3.7 a time-linear change in surface charge can be modelled as a block pulse in the modification current.

$$Q_s(t) = Q_0(r(t) - r(t-T)) \quad \rightarrow \quad I_{mod}(t) = Q_0(u(t) - u(t-T)) \tag{3.8}$$

Where $u(t)$ is the unit step function and $r(t)$ is the ramp function. Equation 3.7 and 3.8 provide a possibility of increasing or decreasing the effective floating gate charge. These equations do not always represent real-time behaviour and need to be redefined per specific application.

3.3 MOSFET modelling

The MOSFET part of the sensor plays an important role in the behaviour of the sensor. Its parameters determine the response in drain current to changes in the floating gate voltage. Since its invention, more and more accurate simulation models have been developed. ADS supports various of these models. The choice was made to begin the model with a LEVEL 3 semi-empirical model which is a mixture of analytical and empirical expressions deemed reliable for channel lengths down to 1 μm [18]. Utilizing the ADS optimization tool, the model parameters were adjusted until the measurement data and the simulated data converged to less than the desired error [19]. Either parameters V_{T0}, k, γ, ϕ, and λ or the process parameters t_{ox}, U_o, N_{sub}, and N_{ss} need to be specified for ADS to determine the DC characteristics of the MOSFET. In addition, parameters η and θ will be extracted. η is the static feedback on the threshold voltage which models the effect of V_{DS} on the threshold voltage. θ is the mobility modulation which describes the effect of V_{GS} on the surface mobility. They are listed in Table 3.2. The full ADS implementation is described in Appendix C. It is also possible for some parameters to be extracted either mathematically or graphically, which is explained in Appendix B.

Table 3.2: Description and units of the parameters governing the DC characteristics of the MOSFET

Parameter	Description	Unit
V_{T0}	zero-bias threshold voltage	V
k	transconductance	A/V^2
γ	bulk threshold	$\sqrt{V}$
ϕ	surface potential	V
λ	channel-length modulation	1/V
t_{ox}	oxide thickness	m
U_o	surface mobility	$cm^2/(Vs)$
N_{sub}	(bulk) doping density	cm^{-3}
N_{ss}	surface state density	cm^{-2}
θ	mobility modulation	1/V
η	static feedback	none

The provided measurement data consisted of a set of I_{DS} as function of V_{DS} for varying V_{GS} and a set of I_{DS} as function of V_{GS} for V_{DS} = 0.5V. First, the latter set was used to obtain V_{T0}. Then, the rest of the parameters were extracted with the first set of measurement data. Alongside the measurement data, process parameter values were given, which can be seen in Table 3.3.

3.4 Sensing area modelling

The goal of this section is to derive an electrical model for the interface between the solution and the floating gate. We first look at the interaction between the surface area oxide and ions in the solution and the Electric Double Layer (EDL) that forms as a consequence of surface charge. We will then look at an

Table 3.3: Description, value and units of the process parameters of the MOSFET

Parameter	Description	Value	Unit
L	channel length	2	µm
W	channel width	15	µm
A_d	drain area	1.17E-10	m^2
A_s	source area	1.17E-10	m^2
P_d	drain perimeter	3.1E-5	m
P_s	source perimeter	3.1E-5	m
N_{rd}	drain squares	4E-6	none
N_{rs}	source squares	4E-6	none
Temp	temperature	25	°C

electrical model for the EDL which allows us to link changes in floating gate voltage (and drain current) to changes in properties of the solution, such as the pH.

Table 3.4: Description and units of parameters related to the sensing area and EDL

Parameter	Description	Unit
K_A	Dissociation constant for reaction 3.9	N.A.
K_B	Dissociation constant for reaction 3.10	N.A.
$[H_S^+]$	proton activity at the oxide surface	$1/\text{m}^2$
$[H_B^+]$	proton concentration in the bulk of the solution	$1/\text{m}^3$
Γ	total number of surface binding sites per unit area	$1/\text{m}^2$
Γ^{0^-}	O$^-$ surface groups per unit area	$1/\text{m}^2$
Γ^{OH}	OH surface groups per unit area	$1/\text{m}^2$
$\Gamma^{\text{OH}_2^+}$	OH$_2^+$ surface groups per unit area	$1/\text{m}^2$
σ_0	charge concentration at the oxide surface	Q/m^2
σ_{DL}	counter-charge against immobilized surface charge	Q/m^2
σ_{ins}	effective surface charge distribution	Q/m^2
Ψ_0	potential at the oxide surface to solution interface	V
Ψ_{DL}	Double layer potential	V
A_S	Sensing area surface	m^2
C_{SG}	Sensing area oxide capacitance	F
C_{Stern}	Double layer capacitance	F
z_i	Ion species i charge number	N.A.
λ_d	Debye length	m

3.4.1 Electric Double Layer (EDL) Theory

Changes in effective gate charge that modulate the drain current are directly related to changes in sensing area surface charge. It is therefore important to take a closer look at the oxide surface that is exposed to the solution to see how these charges are immobilized. When exposed to a solution, the oxide surface is free to interact with H^+ ions in the solution. This interaction can be described using the site-dissociation model [20]. This model is described with the following dissociation reactions:

$$\text{S-OH} \underset{}{\overset{k_A}{\rightleftharpoons}} \text{S-O}^- + \text{H}_S^+ \tag{3.9}$$

and

$$\text{S-OH}_2^+ \overset{k_B}{\rightleftharpoons} \text{S-OH} + \text{H}_S^+ \tag{3.10}$$

In these dissociation reactions, S is the surface group. K_A and K_B are the dissociation constants that determine the equilibrium ratio between both sides of the dissociation equation. Note that the hydroxyl groups here are not negatively charged at the surface. This is because the charges of anions (-O in this case) are neutralized differently at the at the surface of a crystal than at the crystal interior [21]. This leads to broken bonds and consequently charged S-O^- groups that can be neutralized by protons in the solution.
The surface concentrations of the O^-, OH and OH_2^+ are denoted as Γ^{0^-}, Γ^{OH} and $\Gamma^{OH_2^+}$ respectively. The total number of binding sites per surface area unit Γ is the sum of the individual surface group concentrations. As a result, the dissociation constants can be written as in the following equations:

$$K_A = \frac{[H_S^+]\Gamma^{O^-}}{\Gamma^{OH}} \tag{3.11}$$

and

$$K_B = \frac{[H_S^+]\Gamma^{OH}}{\Gamma^{OH_2^+}} \tag{3.12}$$

The immobilized surface charge on the oxide is the sum of the contributing charges from the SO^- and SOH_2^+ surface groups and can be written as a function of the dissociation constants [22].

$$\sigma_0 = -q\Gamma^{0^-} + q\Gamma^{OH_2^+} = \frac{-q\Gamma}{1 + \frac{[H_B^+]}{K_A}} + \frac{q\Gamma}{1 + \frac{K_B}{[H_B^+]}} \tag{3.13}$$

The unknown factor in this equation is the proton concentration at the oxide surface, which can be derived from the Boltzmann expression [23].

$$[H_S^+] = [H_B^+]\text{exp}\Big(\frac{-z_i q \Psi_0}{kT}\Big) \tag{3.14}$$

Here $[H_B^+]$ is the proton concentration in the bulk of the solution, z_i is the ion charge number, which is equal to one and Ψ_0 is the potential at the oxide surface. Note that this expression assumes that the potential of solution bulk is zero, since Ψ_0 is the surface potential relative to the bulk potential. The EDL is formed close to the sensing surface. The EDL consists of an accumulation of counter-ions that functions as a screening layer for the electric field due to the floating gate and the immobilized charge on the surface [16]. This effect is modelled using the Stern model [23]. In this model the system of accumulated counter-ions, located directly against the immobilized surface charges is modelled as a capacitor. The counter-ions themselves are approached as point charges located a the centre of a sphere of finite size with a radius δ, while the immobilized surface charge is modelled as a surface charge distribution. This way, accumulation of counter-ions over the immobilized surface area charges can be modelled as a parallel plate capacitor with a dielectric thickness δ. This capacitor is denoted as C_{Stern}. The relative permittivity of this capacitor is lower than the relative permittivity of water and is estimated to be approximately 10. As a result, the Stern capacitance can be written as follows:

$$C_{Stern} = A_S \frac{10\epsilon_0}{\delta} \tag{3.15}$$

The counter-ion charge that contributes to the voltage drop over the Stern layer is denoted as σ_{DL}. σ_{DL} is smaller in magnitude than the total immobilized charge on the oxide surface σ_0. This is because of two reasons. The first reason is that the immobilized charge distribution is the sum of two charge densities, σ_{ins} and $-\sigma_{DL}$, where σ_{ins} is the charge that contributes to the voltage drop over the surface oxide capacitance. The second reason is that the total double layer screening charge is not all accumulated at the interface. In fact, the counter-ion density diffuses into the bulk of the solution over a distance called the Debye length λ_d. This length is also called the thickness of the diffuse layer and is defined as follows:

$$\lambda_d = \sqrt{\frac{\epsilon_W \epsilon_0 kT}{q^2 \sum n_{i0} z_i^2}} \tag{3.16}$$

Here ϵ_W is the relative permittivity of water and the term $\sum n_{i0} z_i^2$ is the sum of all present ion concentrations and their respective charge number and is determined by the salinity of the solution. σ_{DL} can be written as a function of the Debye length and the potential at the counter-ion plane Ψ_{DL} as is shown in Equation 3.17. This equation is described by the Grahame equation [16], where Ψ_{DL} is defined relative to the potential of the solution bulk.

$$\sigma_{DL} = -\frac{2\epsilon_W \epsilon_0 kT}{q\lambda_d} \sinh\left(\frac{q\Psi_{DL}}{2kT}\right) \tag{3.17}$$

The immobilized charge on the sensing area surface is coupled to the floating gate capacitively via the oxide layer. This capacitance is denoted as C_{SG}. The complete floating gate to solution bulk interface can be modelled as an electrical circuit. The floating gate is coupled to C_{SG} in series with C_{Stern}. The double layer charge σ_{DL} is coupled to the solution bulk via the diffuse layer. The adapted equivalent circuit is shown in figure 3.4.

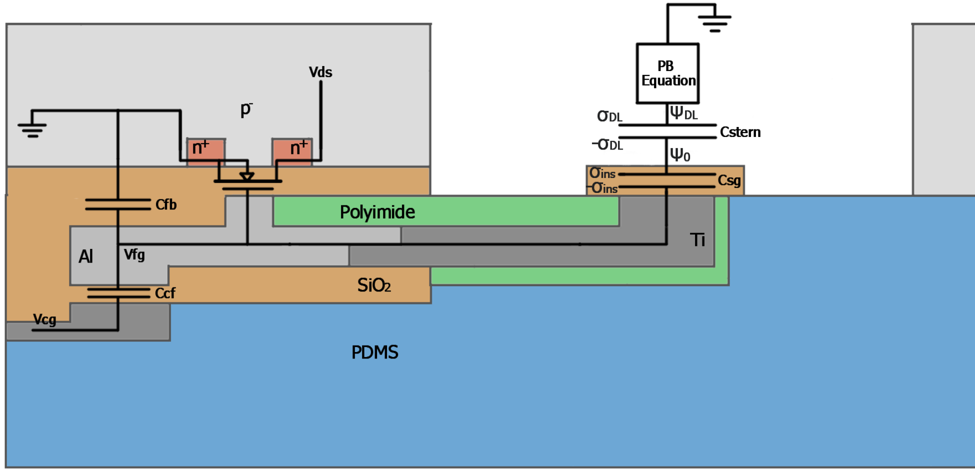

Figure 3.4: Cross section of the ISFGFET sensor and its equivalent circuit, including the electrically equivalent circuit for the sensing gate oxide and the EDL (See Figure 3.1 for comparison)

Note that the effective charge variation in the floating gate is not σ_0 but rather σ_{ins}, which is the surface charge contribution to the potential difference of the C_{SG}. We will refer to this charge distribution as the 'effective surface charge distribution'.

$$\sigma_{ins} = \frac{C_{SG}}{A_S}(\Psi_0 - V_{FG}) = \sigma_0 + \sigma_{DL} \tag{3.18}$$

With the expressions for the charge densities of the oxide surface and double layer, we can write the expressions for the potentials at the oxide surface and at the Stern layer.

$$\Psi_0 = V_{FG} + A_s \frac{\sigma_0 + \sigma_{DL}}{C_{SG}} \tag{3.19}$$

$$\Psi_{DL} = \Psi_0 + A_s \frac{\sigma_{DL}}{C_{Stern}} \tag{3.20}$$

The expression for Ψ_0 is coupled to the floating gate voltage. The formula for the floating gate voltage as in Equation 3.1 is based on the charge redistribution in the floating gate due to immobilized surface charges. As shown in Equation 3.18, $Q_i(Q_s)$ in not equal to $-Q_s$, but rather $-\sigma_{ins} A_S$. σ_{ins} depends on the potential drop over the sensing surface oxide. The floating gate voltage can therefore be written as a function of Ψ_0. This expression is derived using the principle of conservation of charge.

$$Q_{F0} = C_{CF}(V_{FG} - V_{CG}) + C_{FB} V_{FG} + C_{SG}(V_{FG} - \Psi_0) \tag{3.21}$$

Table 3.5: EDL model equations

$\Psi_0 = V_{FG} + A_s \dfrac{\sigma_0 + \sigma_{DL}}{C_{SG}}$	(1)
$\Psi_{DL} = \Psi_0 + A_s \dfrac{\sigma_{DL}}{C_{Stern}}$	(2)
$\sigma_{DL} = -\dfrac{2\epsilon_W \epsilon_0 kT}{q\lambda_d} \sinh\Big(\dfrac{q\Psi_{DL}}{2kT}\Big)$	(3)
$\sigma_0 = \dfrac{-q\Gamma}{1 + \dfrac{[\mathrm{H}_B^+]\exp\Big(\dfrac{-z_i q\Psi_0}{kT}\Big)}{K_A}} + \dfrac{q\Gamma}{1 + \dfrac{K_B}{[\mathrm{H}_B^+]\exp\Big(\dfrac{-z_i q\Psi_0}{kT}\Big)}}$	(4)
$V_{FG} = \dfrac{C_{CF}V_{CG} + C_{SG}\Psi_0 + Q_{F0}}{C_{tot}}$	(5)

$$V_{FG} = \frac{C_{CF}V_{CG} + C_{SG}\Psi_0 + Q_{F0}}{C_{tot}} \tag{3.22}$$

Where C_{tot} is the total floating gate capacitance including the sensing area capacitance. Note that this is different from the total gate capacitance in Section 3.2, where the model is decoupled from the sensing area model and the total floating gate does not include the sensing area capacitance.

3.4.2 EDL modelling

In the previous section, the double layer was described as two capacitors C_{SG} and C_{Stern} connected in series. The double layer charge density σ_{DL} was described by the Grahame equation and the total immobilized surface charge σ_0 was shown to be a function of the oxide surface dissociation constants, then oxide surface potential and the solution bulk pH. These five expression (see Table 3.5) form a system of nonlinear equations that simulate the dynamics of the floating gate to solution interface. This system of equations is identical to the system of equations presented by Kaisti et al. [24], with the exception that no reference electrode is used. The system of equations can be solved in a mathematics based program like Matlab. Matlab code for solving the set is shown in Appendix D and is used for characterizing the surface potential and charge density for different dissociation constants, molarity, pH and floating gate voltage.

In order to validate the combined model of the sensing area, the floating gate and the MOSFET, the system of equations as in table 3.5 needs to be coupled to the model as described in Section 3.2. This is achieved by controlling Ψ_0 and Ψ_{DL} with behavioural voltage source and coupling the system directly to the floating gate. The resulting circuit is shown in Figure 3.5. In ADS, the voltage sources are implemented using Symbolically Defined Devices (SDD's). These elements contain multiple ports that can be used as inputs as well as outputs. Outputs can be defined as a function of input potentials and currents. By setting input currents to zero and defining the output potential as one or multiple input potentials, the element effectively becomes a voltage dependent voltage source that allows for the implementation of a system of nonlinear equation, given that system converges to a DC solution.

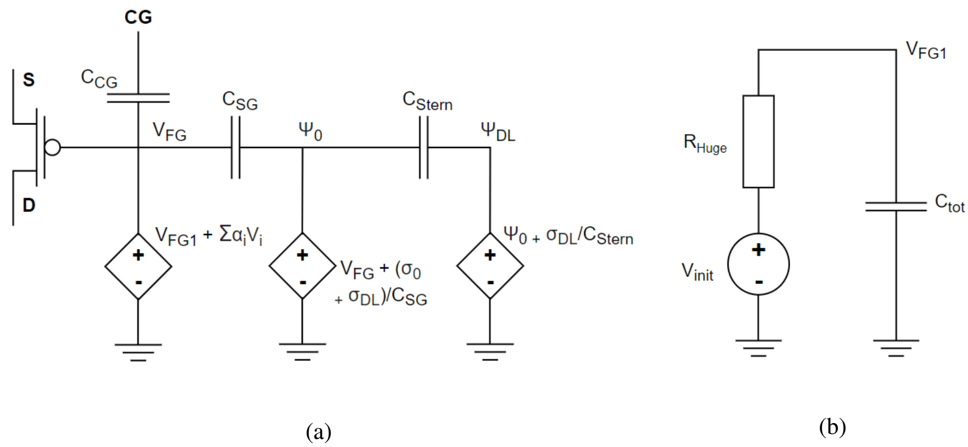

Figure 3.5: (a) Model of a floating gate MOSFET, extended to include the Electric Double Layer model. (b) A second node (FG1) is used again to compute the charge on the floating node. (Compare with Figure 3.3)

Chapter 4

Model Validation

In this chapter, the ISFGFET ADS model is validated with the exception of the sensing area model from Section 3.4.

4.1 ISFGFET Modelling results

As a result of curve-fitting to the output measured characteristics of the ISFGFET with the ADS optimization procedure, parameter values were extracted which are shown in Table 4.1. The simulated ISFGFET using these parameters was compared to the measurement data where the sensor is not exposed to an aqueous solution, which can be seen in Figure 4.1, and the absolute and relative deviations between the two are shown in Figure 4.2 and Figure 4.3 respectively.

Table 4.1: The extracted parameters values as a result of ADS optimization

Parameter	V_{T0}	k	γ	ϕ	θ	η	V_{MAX}
Value	4.648E-1	3.280E-5	1.225E-1	1.141E-1	2.145E-2	1.846E-1	2.719E5
Unit	V	A/V^2	$\sqrt{\text{V}}$	V	1/V	none	V

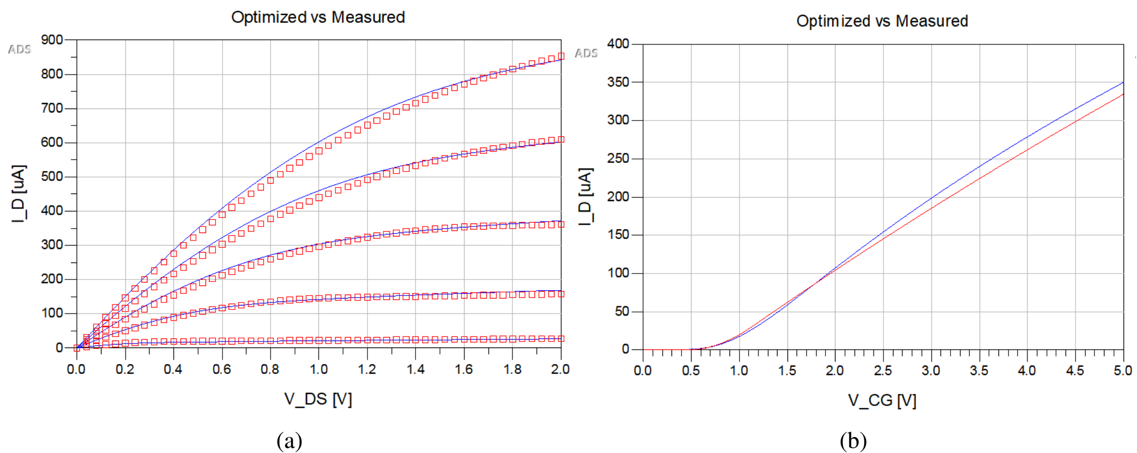

(a) (b)

Figure 4.1: a) A plot of I_D as a function of V_{DS} for various V_{CG}'s for the comparison between the simulated data in red and the measured data in blue. b) A plot of I_D as a function of V_{CG} for the comparison between the simulated data in red and the measured data in blue.

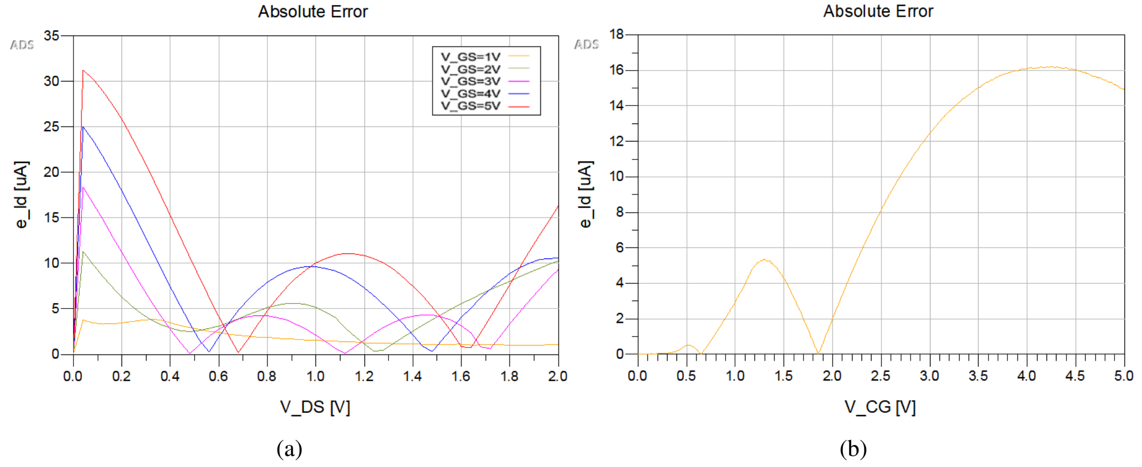

(a) (b)

Figure 4.2: a) The absolute drain current error of Figure 4.1a. b) The absolute drain current error of Figure 4.1b.

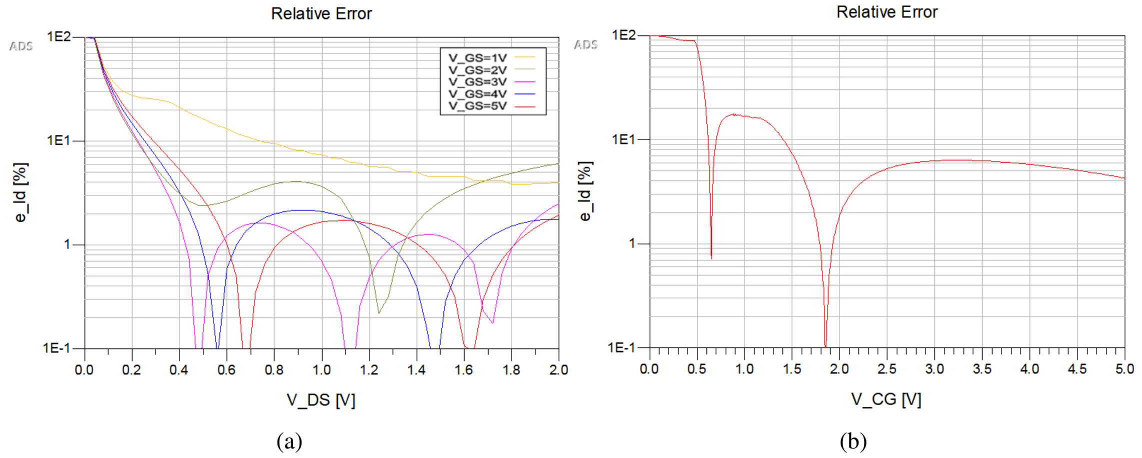

(a) (b)

Figure 4.3: a) The relative drain current error of Figure 4.1a. b) The relative drain current error of Figure 4.1b.

4.2 FGFET Validation discussion

According to the results in the previous sections, the FGFET model without sensing area model is relatively accurate. As shown in Figure 4.3a, the relative error stays under 2% for a substantial range of V_{DS} excluding V_{GS} = 1-2 V. Similarly, Figure 4.3b shows a generous range of V_{CG} where the relative error is beneath 10%. Altogether, the requirements set in Chapter 2 are met and it provides a solid basis for the sensitivity analysis that will be done in the next chapter. Nevertheless, Improvement can be made.
Firstly, only a limited amount of parameters was extracted of the model considering the scope of this thesis. Furthermore, even when all parameters of the chosen model are extracted, a different model with possibly more parameters like the BSIM models could be used to improve accuracy. Ideally, the model is tailored to the fabrication technology.
Secondly, a semi-empirical model was used which isn't analytic. A certain error is to be expected, though computation time is up to 40% faster [27]. It would however be interesting to see how a physics based simulator (like COMSOL) would compare. Additionally, the voltage range and the amount of samples could be increased to aid the fitting process. Furthermore, considering that there are 8 ISFGFETs in total on the sensor, statistics like the variance could be estimated to obtain a baseline.

4.3 Sensing area model validation

A full validation of the model, where the double layer model is included, requires measurements at pH values over the entire pH range. An attempt at validating the full model is made in Section 4.3.2, but due to a discrepancy between simulated sensitivity data and measured data and due to the lack of measurements over the whole pH range, the model was not fully validated.

4.3.1 Conceptual validation

Before attempting to validate the response of the full model in ADS, it is useful to see whether the behaviour of the sensing area model matches that of the models present in earlier literature. We specifically look at the surface potential Ψ_0, since this is the potential that determines, in combination with the sensing area capacitance C_{SG}, the effect of the sensing area model on the floating gate voltage V_{FG}. Figure 4.4 shows the behaviour of Ψ_0 to some parameters that are related to the oxide surface. The exact behaviour of Ψ_0 depends on the interplay between the equations as described in Table 3.5. It is therefore very difficult to fully validate the correctness of the model in this manner, since small changes in the combination of dissociation constant, dielectric permittivity, dielectric thickness, total number of surface binding sites and salinity can completely change the model characteristics.

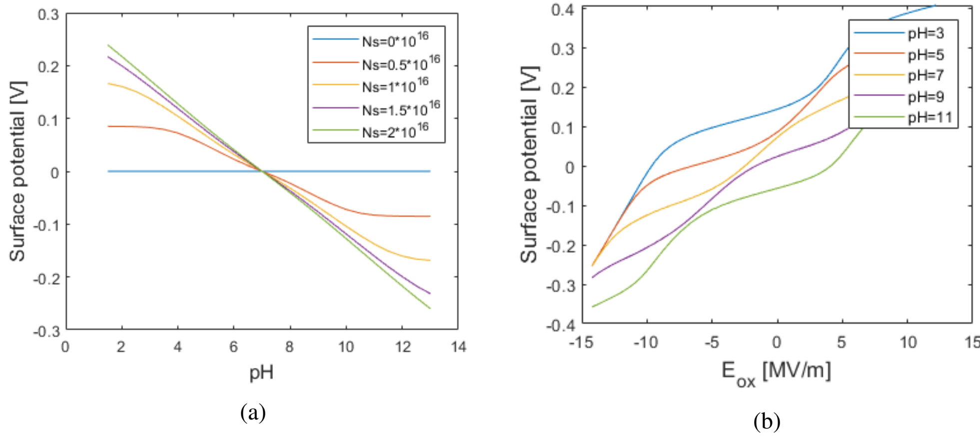

Figure 4.4: Simulated behaviour of the sensing area model in MATLAB. (a) Response of the surface potential Ψ_0 to the pH for different binding site densities. Here $t_{oxSA} = 10nm$, $pK_A = 8$, $pK_B = 6$, $\epsilon_{ox} = 9.3$ and $n_0 = 10mM$ (Identical to the values used by Kaisti et al. [22]). (b) Response of the surface potential Ψ_0 to electric field through the sensing area oxide for different pH values. Here $t_{oxSA} = 50nm$, $pK_A = 5$, $pK_B = 10$, $\epsilon_{ox} = 9.3$ and $n_0 = 10mM$.

Figure 4.4a shows the effect that the total number of surface binding sites has on the response of Ψ_0 to the pH. As expected, in the absence of binding sites, the surface potential is equal to the solution bulk potential, which was earlier assumed to be zero. In accordance with the surface potential behaviour presented by Jayant et al. [25], a high number of surface binding sites is a characteristic of a Nernstian surface. This means that the surface potential varies linearly with the pH. The response of non-Nernstian surfaces potentials does not vary linearly with the pH.
Figure 4.4b shows the manner in which the surface potential varies with the electric field through the oxide for different values of the bulk pH. This behaviour is similar to that of the model described by Kaisti et al. [22]. This characteristic is especially important when varying the control gate voltage, as this can affect the Surface potential non-linearly, leading to a non-linear change in drain current.

4.3.2 Full model validation

The sensing area model is validated in ADS using the earlier extracted MOSFET parameters. In the first measurement utilized for validation, the sensing area is exposed to DI water (pH $\simeq 7$). In the second measurement, the sensing area is exposed to a solution with a pH of 4.1. In both cases, the sensing area is covered by a layer of SiO_2 of $50\,\mathrm{nm}$. Figure C.4 and C.5 in the appendix show the simulated and measured response of the drain current for $V_{CG} = 2V$ and $V_{CG} = 4V$ respectively. As expected, the drain current for pH $= 7$ is lower than the drain current for pH $= 4.1$ due to a lower value of the surface potential Ψ_0. This is the case for the measured data as well as the simulated data. The sensitivity of the simulated data, however, shows a much lower pH sensitivity than the measured data, approximately a factor 10 lower. At the time of writing, a clear cause for this difference has not been found. The simulated bias current is also slightly different from the measured bias current. Unlike the difference in sensitivity, this can be explained by inaccuracies in the MOSFET modelling.

Chapter 5

Sensitivity Analysis

In this section, we will look deeper into the effect of certain parameters of the ISFGFET behaviour. The goal of the sensitivity analysis is to increase the response in drain current to floating gate charge redistribution. Section 5.1 gives a theoretical analysis on which parameters affect the ISFGFET sensitivity. Sections 5.2 until 5.3 discuss the expected effect of changes in the relevant ISFGFET parameters and compare the results to effect that is simulated in the ADS software. Similarly, Section 5.4 discusses the effect of the MOSFET. After discussing the bias point and limitations in Sections 5.6 and 5.5 respectively, a final sensitivity simulation of the MOSFET is shown in Section 5.7. After this the findings of the chapter are discussed in Section 5.8.

5.1 Sensitivity factors

The goal of the sensitivity analysis is to find the factors that contribute most to the sensitivity of the ISFGFET in the saturation region. In this section we will assume that the ISFGFET is biased at a given control gate voltage V_{CG}. An expression for the ISFGFET sensitivity in the saturation region was derived for small charge variations in Section 3.1.

$$\frac{\Delta I_D}{\Delta Q_s} = \frac{2I_{D0}}{C_{CF}V_{CG} - V_{T0}(C_{CF} + C_{FB})} \tag{5.1}$$

Where I_{D0} is the biased saturation drain current and $I_{D0} \gg \Delta I_D$. Using the Unified Model [18], the bias drain current can be expressed as

$$I_{D0} = \alpha(V_{FG} - V_{T0})^2 \qquad \alpha = \frac{\mu_n C_{ox}}{2}\frac{W}{L}(1 + \lambda(V_{DS} - V_{DSAT})) \tag{5.2}$$

By inserting Equation 3.1 into the expression for the bias current and adopting the earlier assumption that $C_{CF}V_{CG} \gg Q_{F0}+Q_s$, Equation 5.2 can be rewritten as Equation 5.3. Consequently, a new expression for the ISFGFET sensitivity is derived in Equation 5.4.

$$I_{D0} = \alpha\Big[\frac{C_{CF}V_{CG}}{C_{CF} + C_{FB}} - V_{T0}\Big]^2 \tag{5.3}$$

$$\frac{\Delta I_D}{\Delta Q_s} = \frac{2\alpha}{(C_{CF} + C_{FB})}\Big[\frac{C_{CF}V_{CG}}{(C_{CF} + C_{FB})} - V_{T0}\Big] \tag{5.4}$$

From this expression of the ISFGFET sensitivity, we can see a number of factors that are important for sensitivity optimization. The most obvious factor is α, which is related to the MOSFET dimensions. Given that the ISFGFET is biased at a fixed control gate voltage V_{CG}, the other parameters that influence the sensitivity are related to the floating gate capacitance. The optimization of the floating gate capacitance is discussed in Section 5.2 and the MOSFET parameter optimization is discussed in Section 5.4. Note that the expression of the ISFGFET as given in Equation 5.4 only shows the sensitivity of the MOSFET

Table 5.1: Description and units of device and material parameters

Parameter	Description	Unit
t_{oxFB}	oxide thickness between floating gate and silicon body	m
t_{oxSA}	oxide thickness between floating gate and measured solution	m
t_{CF}	dielectric thickness of the parallel plate capacitor C_{CF}	m
ϵ_{CF}	dielectric permittivity of the parallel plate capacitor C_{CF}	F/m
ϵ_{ox}	oxide permittivity	F/m
A_{FGC}	floating gate area contributing to C_{CF} and C_{FB}	m^2
A_S	Sensing area surface	m^2

to charge redistribution in the floating gate. It doesn't provide any information about how the sensing area dimensions affect this charge redistribution. The effect of the sensing area dimensions on the sensitivity is discussed in Section 5.3.

5.2 Floating gate capacitance

5.2.1 Optimizing the floating gate capacitance

From Equation 5.4, multiple observations can be made about the effect of the floating-gate capacitance has on the sensitivity. Firstly, the total capacitance consists mainly of the sum of two capacitances, the control gate capacitance C_{CF} and the floating-gate-to-body capacitance C_{FB}. From the expression, it seems beneficial to minimize the sum of C_{CF} and C_{FB} in order to increase the sensitivity of the ISFGFET to effective gate charge variations. However, note that this sum must still be much larger than the sensing area capacitance C_{SG}, such that operation in the MOSFET saturation region is ensured, even when surface charges are immobilized on the sensing area surface. Section 5.3 will discuss the effect of the sensing area capacitance in more detail.

Another observation that can be made from Equation 5.4, is that increasing the term $\frac{C_{CF}}{C_{tot}}$ also increases the ISFGFET sensitivity. Since the factor C_{tot} here is the sum of the control gate capacitance and parasitic capacitances (ignoring the sensing area capacitance for now), this means that any parasitic capacitances should be reduced as much as possible. The largest parasitic capacitance is the floating-gate-to-body capacitance. Reducing this capacitance will result in a factor $\frac{C_{CF}}{C_{tot}}$ that approaches one.

However, it is important to note that C_{FB} is not independent of C_{CF}. The floating-gate-to-body capacitance (see figure 3.1) is located parallel to the control gate capacitance. The same floating gate area A_{FGC} that form a parallel plate capacitor with the control gate also forms a parallel plate capacitor with the silicon substrate. This means that the C_{CF} can be expressed as a function of C_{FB} as shown in Equation 5.5. For simplicity, other parasitic contributions to the floating gate capacitance are not taken into account here.

$$C_{FB} = A_{FGC}\frac{\epsilon_{ox}}{t_{oxFB}} = C_{CF}\frac{t_{CF}}{\epsilon_{CF}}\frac{\epsilon_{ox}}{t_{oxFB}} \tag{5.5}$$

From this equation, it is apparent that the floating-gate-to-body capacitance can be reduced only by increasing the oxide thickness t_{oxFB} since reducing A_{FGC} also reduces C_{CF}. The simulated effect of increasing this oxide thickness is shown in figure 5.1. The sensitivity can be seen to slowly converge to a point where C_{CF} is much larger than the other floating gate capacitances. The maximum oxide thickness is constrained by the layout of the sensor (see Figure 3.4).

5.3 Sensing area parameters

So far, we have not taken the sensing area itself into account for analyzing the sensitivity. The dimension that can be tuned are the surface area and the oxide thickness. These parameters are related to the total

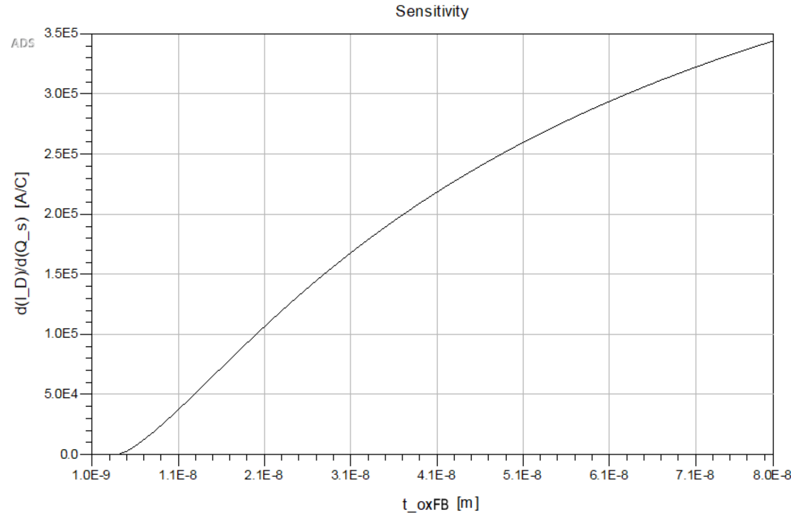

Figure 5.1: The effect of the increasing the oxide thickness t_{oxFB} on the sensitivity of the sensor.

surface charge and to the oxide capacitance. We will, however, also look at the type of oxide that is used for the sensing area. The type of oxide is also related to the capacitance by its relative permittivity. The oxide however also determines the total number of binding sites at the surface and the dissociation constants of the surface-proton interaction.

5.3.1 Dissociation constants

The dissociation constants depend on the type of oxide that is used for C_{SG}. In this thesis, two types of oxide are considered, SiO_2 and TiO2. Typical values for the parameters of these oxides are shown in Table 5.2. Considering the difference in dissociation constants, it is important to analyse what the effect of different dissociation constants on the sensitivity is.

Figure 5.2 shows a simulated response of the floating gate voltage to the pH of the solution. In Figure 5.2a K_A is kept constant and the response for different values of K_B is shown. In Figure 5.2b, K_B is kept constant and the response is shown for different values of K_A. For simplicity, the oxide thickness, salinity, oxide dielectric permittivity and control gate voltage are the same in both plots. Interestingly, the plots show an identical response, implying that the system is very sensitive to the difference in dissociation constants ΔpK. This value is higher for SiO_2.

Note however, that the dissociation constants are not the only important factor when choosing the oxide surface. In the layout, as was shown in Figure 3.1, the SiO_2 layer is fabricated on top of the Ti gate. If the extra SiO_2 layer is not added, the exposed surface of the Ti gate oxidizes. The thickness of this Ti oxide layer is much smaller than the thickness of an explicitly added Si oxide layer ($50\,\mathrm{nm}$ vs $5\,\mathrm{nm}$). These dimension are related to the oxide capacitance C_{SG} and will be discussed in the next section.

Table 5.2: Typical values of dissociation constants for SiO_2 and TiO_2.

Oxide	pKA	pKb	Reference
SiO_2	6	-2	[20]
TiO_2	8	4.5	[31]

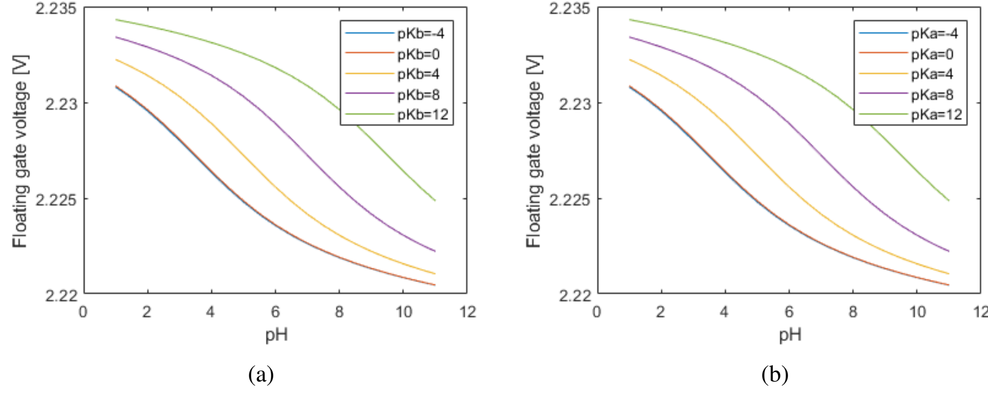

Figure 5.2: Response of the floating gate voltage to the pH of the solution, simulated in Matlab. The control gate voltage is set to 3.3V. The sensing area oxide thickness is $20\,\mathrm{nm}$. (a) Here pKa=6 and the model is evaluated for different values of pKb. (b) Here pKb=6 and the model is evaluated for different values of pKa.

5.3.2 Sensing area capacitance

In Section 5.1, an expression for the sensor drain current in the saturation region to changes in effective gate charge was derived (see Equation 5.6). When a sensing area model is included, the sensor sensitivity can be redefined as the sensitivity to changes in the oxide surface potential Ψ_0.

$$\frac{\Delta I_D}{\Delta \Psi_0} = \frac{2\alpha C_{SG}}{C_{tot}}\left[\frac{C_{CF}V_{CG}}{C_{tot}} - V_{T0}\right] \tag{5.6}$$

Using the previous assumption that $C_{CF} + C_{FB} \gg C_{SG}$, it is straightforward to see that the sensitivity to changes in the oxide surface potential scales directly with C_{SG}. This does however not provide much insight, because it does not explain how Ψ_0 scales with changes in ion concentration.
By expanding the expression the sensing area oxide capacitance C_{SG}, the sensing surface potential Ψ_0 can be written as a function of the oxide dimensions and permittivity. This is shown in Equation 5.7.

$$\Psi_0 = V_{FG} + A_s\frac{\sigma_0 + \sigma_{DL}}{C_{SG}} = V_{FG} + \frac{t_{oxSA}}{\epsilon_{oxSA}}(\sigma_0 + \sigma_{DL}) \tag{5.7}$$

Equation 5.7 seems to suggest that the scaling the sensing area surface has no effect on the surface potential and that the surface potential will scale linearly with the oxide thickness. Figure 5.3, however, shows that this is not the case. The figure shows a typical response of both the surface potential and the effective surface charge to the pH of the solution for three scenarios. (a) shows a reference simulation, (b) shows the same simulation, but C_{SG} is increased by reducing the oxide thickness. (c) also shows the same simulation, but C_{SG} is increased by increasing the surface area.
Figure 5.3b shows that scaling the oxide thickness on the sensing area only scales the surface potential very slightly. Furthermore, Figure 5.3b shows that this is because the effective surface charge *does* scale with the oxide thickness, effectively compensating for the increase in Ψ_0 that would have occurred otherwise. The change in effective surface charge can be explained by the electric field through the oxide. Reducing the oxide thickness increases this electric field which, in turn, 'discourages' protons in the solution from binding at the oxide surface. Figure 5.3c shows that scaling the oxide surface area does not affect the surface potential, which is in accordance with Equation 5.7.
The results from Figure 5.3 suggest that the influence of the scaling on the sensitivity of the sensor is minimal. The sensitivity can be increased both by reducing the oxide thickness and by increasing the surface area. However, keep in mind that there are practical limitations to increasing the surface area. These limitations are determined by the application of the sensor and are set by the necessary area resolution of the measured bio(chemical) environment.

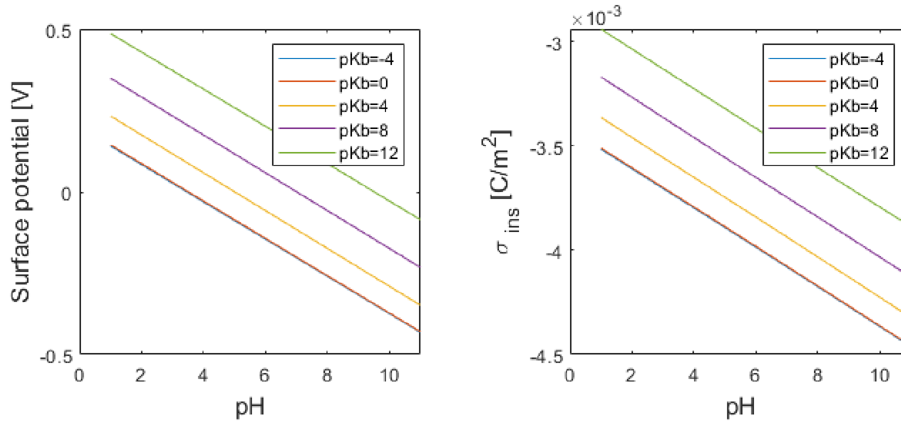

(a) No C_{SG} Scaling

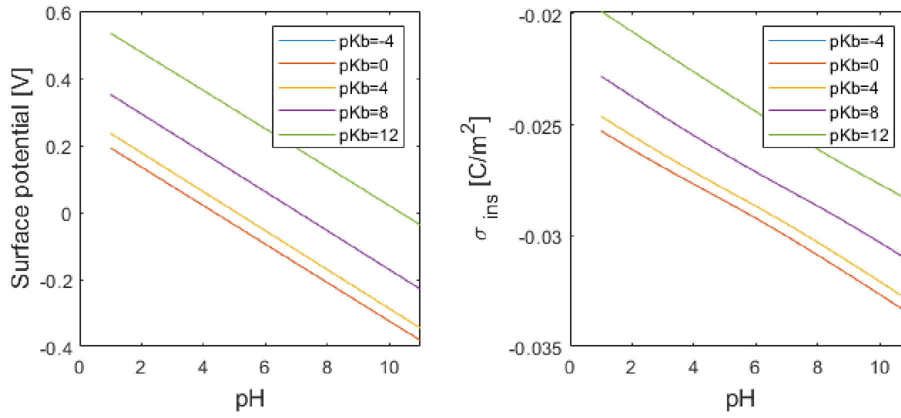

(b) $t_{ox_new} = 0.1 * t_{ox}$

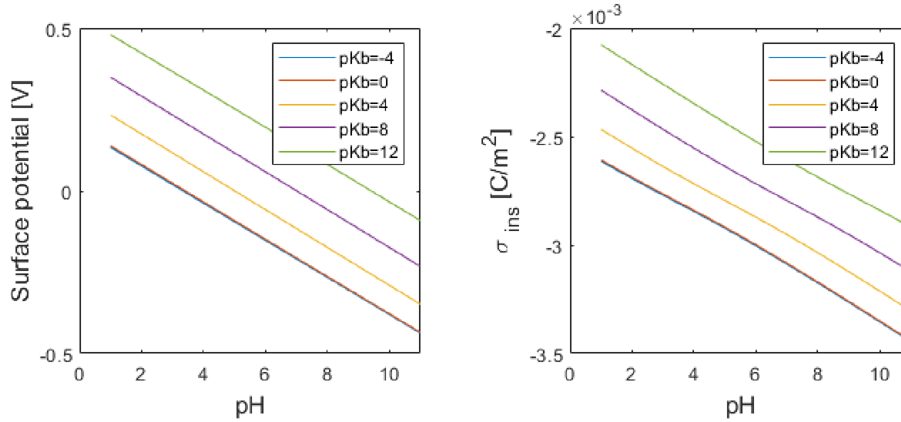

(c) $A_{S_new} = 10 * A_S$

Figure 5.3: Response of the surface potential Ψ_0 and the effective surface charge σ_{ins} to the pH of the solution, simulated in MATLAB. In Figure b and c, the sensing area capacitance C_{SG} has been scaled to be ten times its original value in Figure a, using a different scaling method for each picture. The control gate voltage is set to 3.3V. The sensing area oxide thickness is 20 nm. In each picture, pKa is set to 6 and the model is evaluated for different values of pKb. (b) C_{SG} is scaled by reducing the oxide thickness. (c) C_{SG} is scaled by increasing the surface area.

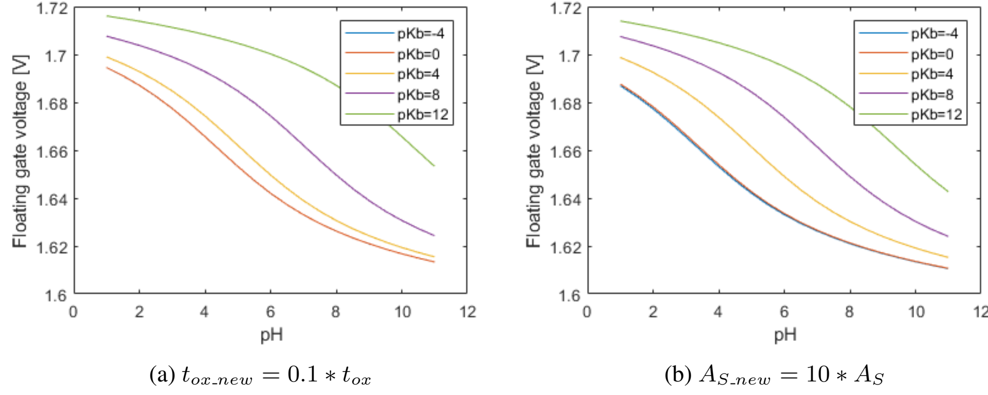

(a) $t_{ox_new} = 0.1 * t_{ox}$ (b) $A_{S_new} = 10 * A_S$

Figure 5.4: Response of the floating gate voltage to the pH of the solution, simulated in MATLAB. In both figures, the sensing area capacitance C_{SG} has been scaled to be ten times its original value in Figure 5.2a, using a different scaling method for each picture (compare with figure 5.2a). The control gate voltage is set to 3.3V. The sensing area oxide thickness is 20nm. pKa is set to 6. (a) Here pKa=6 and the model is evaluated for different values of pKb. C_{SG} is scaled by reducing the oxide thickness. The plots for pKb=-4 and pKb=0 fully overlap, making pKb=-4 invisible. (b) Here pKb=6 and the model is evaluated for different values of pKa. C_{SG} is scaled by increasing the surface area.

5.4 MOSFET parameters

Among the sensitivity influences is of course also that of the MOSFET. In Section 3.3 a semi-empirical model is was decided upon, therefore caution has to be taken as a 1:1 mapping isn't necessarily obtained. Nevertheless, the focus of this section lies on the equations provided by Vladimirescu et al. that from the basis of the SPICE level 3 model [27].
From Equation 5.8, the saturation current, it can be seen that increasing the channel width W will have beneficial effects. Furthermore, C_{ox} can be increased by decreasing t_{ox} or increasing ϵ_{ox} which also produces desired effects. Moreover, voltages V_{GS}, V_{MAX} and V_{DSAT} can be raised while V_{TH} can be lowered. However, V_{MAX} is a curve-fitting parameter, hence its dependencies are unclear from this model. Alongside these voltages is also F_B , the Taylor series expansion coefficient of bulk charge as given by Equation 5.10; Its effect will be discussed later.

$$I^0_{DS} = WC_{ox}[V_{GS} - V_{TH} - (1 + F_B)V_{DSAT}]V_{MAX} \tag{5.8}$$

Firstly, the influence on V_{DSAT} can be observed from Equation 5.9. Note how the first two terms reappear under the square root; It is of a Pythagorean form $a + b - c$. If the triangle inequality is applied, which states that $|c| < |a| + |b|$, it can be concluded that V_{DSAT} is positive and the difference is $2ab$. In essence, this tells us that the first two terms must be the focus of the maximization. V_{DSAT} is multiplied by $(1 + F_B)$ in Equation 5.8 resulting in $V_{GS} - V_{TH} + V_{MAX}L(1 + F_B)/\mu_S$. μ_S is the surface mobility modulation influenced by the gate voltage and can be seen in Equation 5.11. Thus the surface mobility U_0 must be decreased, while F_B must be increased. L will reappear in more equations, though its impact is likely a decrease in sensitivity when enlarged. From this point onwards, more and more parameters become nested in the series of equations. It is more effective to give some graphical representations of the influence the parameters have which will be done in Section 5.7.

$$V_{DSAT} = \frac{V_{GS} - V_{TH}}{1 + F_B} + \frac{V_{MAX}L}{\mu_S} - \sqrt{(\frac{V_{GS} - V_{TH}}{1 + F_B})^2 + (\frac{V_{MAX}L}{\mu_S})^2} \tag{5.9}$$

$$F_B = \frac{\gamma F_S}{4\sqrt{2\phi_F - V_{BS}}} + F_N \tag{5.10}$$

$$\mu_S = \frac{U_0}{1 + \theta(V_{GS} - V_{TH})} \tag{5.11}$$

Besides maximizing V_{DSAT} to obtain more sensitivity, an low as possible V_{TH} is also beneficial. Equation 5.12 tells us about its influences.

$$V_{TH} = V_{FB} + 2\phi_F - \sigma V_{DS} + \gamma F_S F_F(V_{BS}) + F_N(F_F(V_{BS}))^2 \tag{5.12}$$

Where σ is the coefficient of static feedback given by Equation 5.15, F_N is the correction factor of narrow channel effect given by Equation 5.18, F_S is the correction factor of short channel of effect given by Equation 5.19, F_F is a multiplicative factor of the depletion-charge formulation given by Equation 5.17 , γ is the bulk threshold parameter given by Equation 5.13, V_{FB} is the flatband voltage given by Equation 5.16, ϕ_F is the surface potential at strong inversion given by Equation 5.14, and V_{BS} is the substrate to source voltage.

$$\gamma = \frac{\sqrt{2q\epsilon_{si}N_{SUB}}}{C_{ox}} \tag{5.13}$$

$$\phi_F = \frac{kT}{q}\ln\frac{N_{SUB}}{n_i} \tag{5.14}$$

Where n_i is the intrinsic concentration of electrons.

$$\sigma = \eta\frac{\Omega}{C_{ox}L^3} \tag{5.15}$$

Where Ω = 8.15E-22 Fm is an empirical constant.

$$V_{FB} = \phi_{MS} - \frac{qN_{SS}}{C_{ox}} \tag{5.16}$$

Where ϕ_{MS} is the metal (poly-silicon) semiconductor work function difference.

$$F_F(V_{BS}) = \frac{\sqrt{2\phi_F}}{1 + V_{BS}/4\phi_F} \tag{5.17}$$

$$F_N = \delta\frac{\pi\epsilon_{si}}{2C_{ox}W} \tag{5.18}$$

$$F_S = 1 - \frac{X_J}{L}[\frac{L_D + W_C}{X_J}\sqrt{1 - (\frac{W_P/X_J}{1 + W_P/X_J})^2} - \frac{L_D}{X_J}] \tag{5.19}$$

Where L_D is the lateral diffusion length, W_P is the depletion layer width of a plane junction. W_C is the depletion layer width of a cylindrical junction and X_J is the metallurgical junction depth. L_D, X_J and L are parameters representing the physical measures of the materials. In contrast, W_P and W_C need to be determined. W_P is given by Equation 5.20 and W_C is given by Equation 5.21. All the aforementioned parameters relate to the devices geometry and are indicated in Figure 5.5.

$$W_P = X_D\sqrt{2\phi_F - V_{BS}} \tag{5.20}$$

Where X_D is the coefficient of depletion layer width given by Equation 5.22

$$W_C = X_J(d_0 + d_1\frac{W_P}{X_J} + d_2(\frac{W_P}{X_J})^2) \tag{5.21}$$

With empirical constants: d_0 = 0.0631353, d_1 = 0.8013292, d_2 = -0.01110777.

$$X_D = \sqrt{\frac{2\epsilon_{si}}{qN_{SUB}}} \tag{5.22}$$

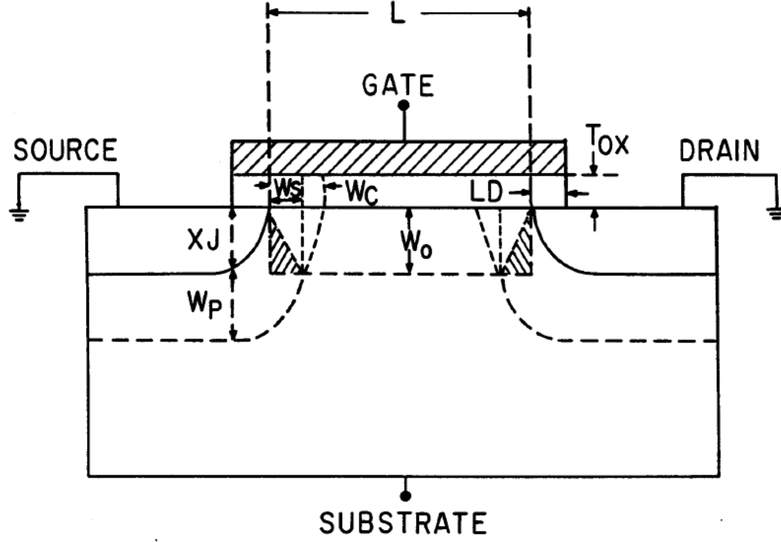

Figure 5.5: Cross section of a level 3 MOSFET with its relevant geometrical parameters [27].

Ideally, the channel length modulation λ has to be minimized to have a flat sensitivity around the bias point. This means that the channel length reduction ΔL given in Equation 5.23 has to go to zero. The reduced form is shown in Equation 5.25 and it can be seen that X_D needs to be a small as possible.

$$\Delta L = \sqrt{(\frac{X_D^2 E_p}{2})^2 + \kappa X_D^2 (V_{DS} - V_{DSAT})} - \frac{X_D^2 E_p}{2} \tag{5.23}$$

Where E_p is the lateral field at channel pinch-off point as given by Equation 5.24.

$$E_p = \frac{I_{DSAT}}{G_{DSAT} L} \tag{5.24}$$

Where I_{DSAT} is the drain current at saturation and G_{DSAT} is the drain conductance at saturation.

$$\kappa X_D^2 (V_{DS} - V_{DSAT}) = 0 \tag{5.25}$$

Temperature scaling also impacts the transistor. The measurement data was obtained outside an incubator, thus during the sensitivity analysis the T_{rise} parameter, which is defined as the temperature rise above ambient, was set to 12°C in order to estimate the performance inside an incubator at 37°C.

No AC analysis is done in this thesis, however, a rough estimate of the cutoff frequency can be made with Equation 5.26 [26].

$$f_T = \frac{\mu_{EFF}(V_{GS} - V_{TH})}{2\pi L^2} \tag{5.26}$$

Where μ_{EFF} is the saturation velocity of hot electrons given by Equation 5.27.

$$\mu_{EFF} = \frac{\mu_S}{1 + \frac{\mu_S}{V_{MAX} L} V_{DS}} \tag{5.27}$$

5.5 Limiting factors

In reality, one can not always fulfill the solution obtained from an optimized model. It can lay out of the bounds. Likewise, the parameters of the ISFGFET are limited by the adopted fabrication technology. First off, the lateral resolution of the layer is dictated by the lithographic resolution of the stepper. In our case that limit is approximately $0.5\,\mu\text{m}$.

Aside from lateral resolution, the thickness of the dielectric layer between floating-gate and control-gate is also capped. Beneath $40\,\mathrm{nm}$, deposition with Plasma Enhanced Chemical Vapor Deposition (PECVD) with eight stations will not result in uniform layers, resulting in possible leakage. Besides resolution, there is also a material constraint. So called 'contaminated' materials such as gold, platinum, etc. do not fit the criterion of CMOS compatibility.
At last, the Varian e500hp implanter that was utilized can provide at least doping concentrations between $9 \times 10^{11}\,\mathrm{ions/cm^2}$ and $1 \times 10^{16}\,\mathrm{ions/cm^2}$ and its energies range from $5\,\mathrm{keV}$ to $150\,\mathrm{keV}$.

5.6 Bias point selection

When measuring the change in drain current over time for an experiment, one does not constantly sweep V_{DS} and V_{CG}. These voltages will typically be fixed at a certain bias point. In order to reliably detect changes in charge for the selected bias point, a high sensitivity is required. Additionally, a stable flat sensitivity across a certain voltage range is necessitated to mitigate the effect of noise on the measurement. This is why the saturation region is recommended for measuring with this type of sensor.
Based on Equation 5.1, it can be seen that the sensitivity is proportional to V_{DS} and V_{CG}. This relation is exhibited in Figure 5.6. However, there is a limit since high electric fields introduce additional electrical characteristics, such as oxide and avalanche breakdown, Fowler-Nordheim tunneling (Subsection 5.6.1) and hot electron injection (Subsection 5.6.2).
Aside from the parasitic characteristics, constraints on supply voltages were also set by the group working around electronics driving the sensor. On the discovery board, the DAC can only supply a maximum of $3.3\,\mathrm{V}$ for V_{CG} and V_{DS} has a limit of $1.65\,\mathrm{V}$ in order to comply with the ADC input requirements after amplification [3]. Moreover considering that our model is only validated up to a V_{DS} of $2\,\mathrm{V}$ and a V_{CG} of $5\,\mathrm{V}$, it would be less representative of reality to cross those soft bounds. Another point to take into account is that the interconnects of the sensor are in the range of a few mm's resulting in a small voltage drop over the wires effectively lowering the bias point of the sensor.
Taking into account the aforementioned considerations, the bias point is taken on a V_{DS} of $1.65\,\mathrm{V}$ and a V_{CG} of $3\,\mathrm{V}$. Assuming that breakdown and tunneling effects are still insignificant for these relatively small voltages.

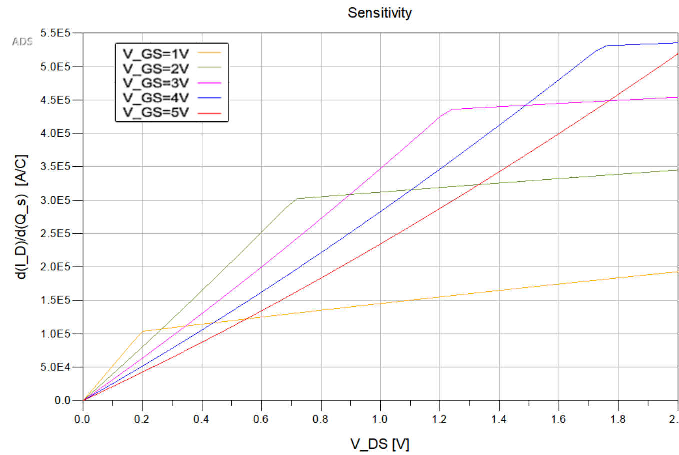

Figure 5.6: A plot of sensitivity as a function of V_{DS} for various V_{GS}'s with the sensitivity being a function of the change in drain current divided by a change in charge of $0.3\,\mathrm{pC}$.

5.6.1 Fowler-Nordheim tunneling

If the barrier of an insulator is thin enough for a given strong electric field, electrons can tunnel through in the direction of that electric field. This means that if V_{CG} is large, it is possible for charges to escape the

floating gate, intermingling with the measurements. The effect of Fowler-Nordheim tunneling is described in Equation 5.28 [29].

$$J = \frac{q^3 E^2}{8\pi h \Phi} \exp[-\frac{4}{3}\frac{\sqrt{2m}\Phi^{3/2}}{\hbar q E}] \tag{5.28}$$

where h = Planck's constant, q = electronic charge, E = electric field, Φ = barrier height, and m = free-electron mass. Relevant parameters can be substituted in Equation 5.28 to obtain Equation 5.29.

$$I = A_{GS}\frac{q^3 V_{FG}^2}{8\pi h \Phi t_{ox}^2} \exp[-\frac{4}{3}\frac{\sqrt{2m}\Phi^{3/2} t_{ox}}{\hbar q V_{FG}}] \tag{5.29}$$

Given that I must be minimized to improve measurement quality, several measures can be taken; The gate oxide t_{ox} can be thickened or its area A can be reduced. Naturally, the voltage applied across the gate can be decreased. However, these countermeasures are inversely proportional to several sensitivity parameters, so an optimum has to be established.
In reality, the theoretical and experimental parameters are extracted, since the determination of FN parameters is still subject to discussion [30]. J. Ranuárez et al. mentions that the Fowler–Nordheim model is not enough to account for effects such as [30]:

- Direct tunneling; At low electric fields the barrier is approximately trapezoidal and not negligible anymore when combined with an oxide thickness of a few nanometers.
- Inversion/accumulation layer carrier quantization.
- Tunneling mechanisms besides conduction band tunneling of electron such as valence band hole tunneling and valence band electron tunneling.
- Tunneling carrier availability response to finite temperature
- Depletion effects on the poly-silicon gate.
- Gate current partitioning
- Image force induced barrier lowering.

Unfortunately, an extensive analysis of tunneling effect and their parameter extractions falls out of the scope of this thesis. A rough estimation was made and the results are shown in Figure 5.7. It can be seen that for L = 2 µm, W = 15 µm and t_{ox} = 45 nm, the tunneling current is not even touching the order of pA's for large V_{CG}'s. But when L = 0.5 µm, W = 3.75 µm and t_{ox} = 10 nm is taken however, the tunneling current is surpassing the order of pA's for a range of V_{CG} close to that of the bias point. Hence, it's recommended to reevaluate the tunneling current when scaling down the gate area and the oxide thickness.

5.6.2 Hot electron injection

Similarly to FN tunneling, when an electron inside a strong electric field builds up enough kinetic energy, it can tunnel through an oxide insulator. This means that charge can get trapped on the floating gate , disturbing the measurement, especially for cases where $V_{GS} < V_{DS}$. Ning et al. [28] determined voltage limits for devices with a minimum channel length of 1 µm. These values are shown in Figure 5.8. It has to be noted however that the assumption is made that 30% of transconductance degradation Δg_m is permissible in 3000 hrs of equivalent DC lifetime. These long-term stress effects may lead to the reevaluation of the bias point after several months of usage when high voltages are used.

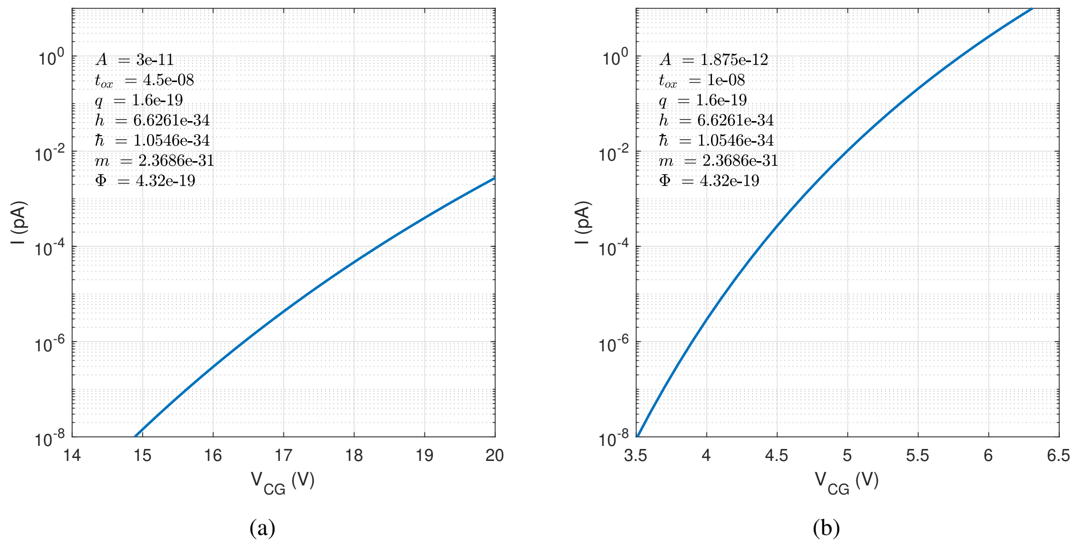

Figure 5.7: a) Fowler-Nordheim tunneling current as a function of the control gate voltage with estimated parameters for the existent sensor b) Fowler-Nordheim tunneling current as a function of the control gate voltage with estimated parameters for a smaller sensor.

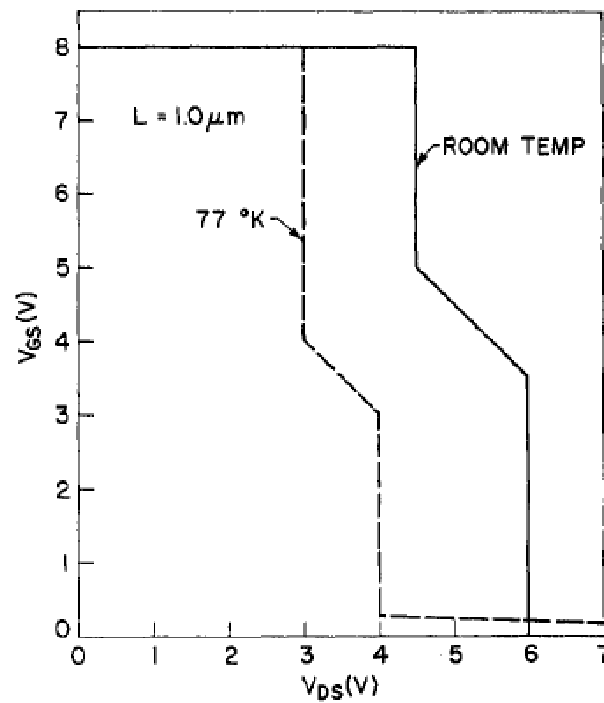

Figure 5.8: Channel hot-electron limits for the L_{eff} = 1.0 μm devices [28]

5.7 Simulation results

Most of the parameter are fixed by the technology. Based on the analysis in Section 5.4 and Section 5.2, some remaining parameters will be adjusted in the simulation model in order to obtain an elevated sensitivity at the prescribed bias point following from Section 5.6. In Table 5.3 the sensitivity of the parameters W, L, t_{ox}, t_{oxFB} and V_{BS} is evaluated. Starting from the left column, their original values are listed together with their determined sensitivity, whereafter each parameter was changed individually while recording their corresponding sensitivity. Finally, a composition of the optimal parameters is given in the right most column. Through the ADS tuning capability the highest sensitivity of 4.56×10^6 A/C was achieved using $L = 0.8\,\mu\text{m}$ en $W = 350\,\mu\text{m}$ assuming that the simulation scales up correctly.

Table 5.3: The original, proposed and optimal value of parameters W, L, t_{ox} and t_{oxFB} with their corresponding sensitivity [A/C] at a V_{DS} of 1.65 V and a V_{CG} of 3 V.

	Original		Proposed				Optimal
	value	sensitivity	value	sensitivity	value	sensitivity	
W	15 µm	4.88×10^5	25 µm	7.69×10^5	50 µm	1.47×10^6	50 µm
L	2 µm		1 µm	7.32×10^5	0.5 µm	7.71×10^5	0.5 µm
t_{ox}	104 nm		75 nm	4.85×10^5	50 nm	4.82×10^5	104 nm
t_{oxFB}	210 nm		104 nm	3.90×10^5	48 nm	2.48×10^5	210 nm
V_{BS}	0 V		1 V	3.38×10^5	-0.25 V	4.69×10^5	-0.25 V

5.8 Sensitivity discussion

As a result of the this chapter, optimal values for the FGFET were obtained in the previous section. Ideally, the MOSFET is wide and narrow. Besides that, V_{BS} can also be manipulated, although beneficial effects were observed to cease beyond -0.25 V. It should be noted that the saturation region also shifted a bit, hence the slightly lower sensitivity. Likewise when t_{ox} is decreased, which increases the value of C_{ox}, the saturation region starts at a higher V_{DS} due to a lower V_{DSAT}. So at the current bias point, the value of t_{ox} is already sufficient. Parameters N_{SUB}, N_{SS} and X_J did not show any influence in the sensitivity simulation when adjusted. This is probably due to the parameters being overridden by the empirical equivalent. Finally, increasing the values of t_{oxFB} and C_{SG} will also provide beneficial effects.

Chapter 6

Conclusion

6.1 Conclusion

Monitoring of cell cultures in real-time can vastly deepen our knowledge on the effect of either diseases or drugs on the targeted organ cells. Since biologists have expressed their need for a portable parameter analyzers for OoC applications, three projects have were set up to come up with a viable design. For correct characterization of the sensing behaviour of the Organ-On-Chip system Portable Analyzer, the requirement for the development of an accurate model of the provided ISFGFET was set, which was the main topic of this thesis. We therefore developed a SPICE-compatible model where the effect of immobilized surface charges on the floating gate voltage is modelled as changes in the effective floating gate voltage. This model was implemented in ADS and subsequently validated using 'dry case' measurements. The model was found to be sufficiently accurate. However, this model is unable to predict expected effective charge variations within the floating gate. Therefore, a SPICE-compatible extension to the model was implemented which simulates the double layer behaviour at the oxide as an electrical circuit and consequently adds the ability to predict effective charge variations.
The conceptual function of double layer model extension was validated and found to show similar behaviour to other earlier implementations of double layer models as an electrical circuit in literature. The sensitivity of the implemented model did, however, not match the sensitivity of measurement data. Attempts to identify the cause of this discrepancy were unsuccessful.
Despite the sensitivity inaccuracy, the double layer model extension did provide useful information on how to optimize the sensing area oxide capacity, with the goal of maximizing the sensitivity to changes in the pH of the solution. It was found that increasing the sensing area oxide capacitance by either decreasing the oxide thickness or increasing the sensing area surface yields similar results.
Furthermore an analysis on the effect of the control gate capacitance on the sensitivity of the sensor provided useful insights on the optimal dielectric thickness of dielectric thickness of the control gate capacitance and the oxide thickness between the floating gate and substrate. An analysis of the bias point provided ideal values for the control gate voltage and the drain-source voltage of the MOSFET. The results of this thesis can be used for characterizing implementations of ISFGFET's with different dimensions as well as the sensitivity optimization in future ISFGFET implementations.

6.2 Recommendations

Due to COVID-19 no physical demonstrator was allowed to be build. Hence, assembling a system based on the work of all three groups is certainly advocated. Important elements to increase the sensitivity of the ISFGFET are the channel width and length of the MOSFET within. $L = 0.8\,\mu\text{m}$ and $W = 350\,\mu\text{m}$ are proposed. It is also recommended to lift the constraint on the supply voltages in order to take a bias point with a higher sensitivity. A lot of potential is to be gained in the refinement of the sensing area model. The relation between the change in the properties of the solution, such as the pH, and changes in drain current is a stepping stone to getting more insight of the effect of for example drugs on the metabolism of the

organ cells. Besides the simulation of the DC characteristics, AC analysis too could be incorporated into the model in order to obtain a measure of reliability when the changes in the composition of the solution change more rapidly. In case that the model presented is not sufficient for AC analysis, the MOSFET model should be interchanged with a more elaborate model such as BSIM coupled with compact modeling procedures.
For future modelling attempts, physics based software could be utilized for comparison to the electrical circuit implementation of the double layer model as well as a more accurate MOSFET model. A noise analysis should be performed to see whether the optimization proposed in this thesis has any draw-backs.

Bibliography

[1] M. Mastrangeli, S. Millet and J. van den Eijnden-van Raaij, ”Organ-on-chip in development: Towards a roadmap for organs-on-chip”, ALTEX, pp. 650-668, 2019. Available: 10.14573/altex.1908271.

[2] H. Aydogmus et al., in preparation (2020)

[3] E. Albayrak and M. Mens, ”Portable Parameter Analyser for Organs-on-Chip: Power Budget Analysis”, Bachelor’s thesis, Delft University of Technology, June 2020.

[4] J. Noordhoek and Y. Wesseling, ”Portable Parameter Analyser for Organs-on-Chip: Calibration & GUI”, Bachelor’s thesis, Delft University of Technology, June 2020.

[5] P. Bergveld, ”Development of an Ion-Sensitive Solid-State Device for Neurophysiological Measurements”, IEEE Transactions on Bio-medical Engineering, vol. 17, p. 70, 1970.

[6] van Hal, R.E.G, J.C.T Eijkel, and P Bergveld, “A Novel Description of Isfet Sensitivity with the Buffer Capacity and Double-Layer Capacitance As Key Parameters”, Sensors & Actuators B: Chemical, vol. 25, pp. 201–205, 1995.

[7] P. Bergveld, “The impact of MOSFET-based sensors”, Sensors & Actuators, vol. 8, pp. 109–127, 1985.

[8] P. Bergveld, “Thirty years of ISFETOLOGY What happened in the past 30 years and what may happen in the next 30 years”, vol. 88, pp. 1–20, 2003.

[9] M. Barbaro, A. Bonfiglio and L. Raffo, ”A charge-modulated FET for detection of biomolecular processes: conception, modeling, and simulation”, IEEE Transactions on Electron Devices, vol. 53, no. 1, pp. 158-166, 2006. Available: 10.1109/ted.2005.860659.

[10] S. Lai , M. Demelas , G. Casula , P. Cosseddu , M. Barbaro , and A. Bonfiglio, ”Ultralow Voltage, OTFT-Based Sensor for Label-Free DNA Detection” Advanced materials, vol. 25, pp. 103-107, 2013.

[11] M. Demelas, S. Lai, G. Casula, E. Scavetta, M. Barbaro, A. Bonfiglio, ”An organic, charge-modulated field effect transistor for DNA detection”, Sensors and Actuators B: Chemical, vol. 171-172, pp. 198-203, 2012.

[12] A. Caboni, E. Orgiu, E. Scavetta, M. Barbaro and A. Bonfiglio, ”Organic-based sensor for chemical detection in aqueous solution”, Applied Physics Letters, vol. 95, no. 12, p. 123304, 2009. Available: 10.1063/1.3232252.

[13] B. Chen, A. Parashar and S. Pandey, ”Folded Floating-Gate CMOS Biosensor for the Detection of Charged Biochemical Molecules”, IEEE Sensors Journal, vol. 11, no. 11, pp. 2906-2910, 2011. Available: 10.1109/jsen.2011.2149514.

[14] Q. Zhang, H. S. Majumdar, M. Kaisti, A. Prabhu, A. Ivaska, R. Österbacka, A. Rahman, and K. Levon, ”Surface Functionalization of Ion-Sensitive Floating-Gate Field-Effect Transistors With Organic Electronics”, IEEE Transactions on Electron Devices, vol. 62, no. 4, pp. 1291-1298, 2015.

[15] A. Spanu, S. Lai, P. Cosseddu, M. Tedesco, S. Martinoia and A. Bonfiglio, ”An organic transistor-based system for reference-less electrophysiological monitoring of excitable cells”, Scientific Reports, vol. 5, no. 1, 2015. Available: 10.1038/srep08807.

[16] Z. Jiang and D. Stein, ”Electrofluidic Gating of a Chemically Reactive Surface”, Langmuir : the ACS journal of surfaces and colloids, vol. 26, no. 17, pp. 8161-8173, 2010.

[17] Rapp, Steven Joseph, ”A Comprehensive Simulation Model for Floating Gate Transistors”; (2010). Graduate Thesis, Dissertations, and Problem Reports. 3064.

[18] J. Rabaey, A. Chandrakasan and B. Nikolic, *Digital integrated circuits.* Chennai: Pearson, 2016, pp 87-130.

[19] F. Peternella, L. Manera and J. Diniz, ”An improved parameter extraction method using an RF software simulation”, 2006. Available: https://sbmicro.org.br/sforum-eventos/sforum2006/8.pdf.

[20] R.E.G. van Hal, J.C.T. Eijkel, P. Bergveld, ”A general model to describe the electrostatic potential at electrolyte oxide interfaces”, Advances in Colloid and Interface Science, vol 69, pp. 31-62, 1996.

[21] T. Hiemstra, W.H. van Riemsdijk and G.H. Bolt, ”Multisite Proton Adsorption Modeling at the Solid/-Solution Interface of (Hydr)oxides: A New Approach I.”, Journal of Colloid and Interface Science, vol. 133, no. 1, pp. 91-104, 1989.

[22] M. Kaisti, Q. Zhang, A. Prabhu, A. Lehmusvuori, A. Rahman, and K. Levon, ”An Ion-Sensitive Floating Gate FET Model: Operating Principles and Electrofluidic Gating”, IEEE Transactions on Electron Devices, vol. 62, no. 8, pp. 2628-2635, 2015.

[23] M. Elimelech, J. Gregory, X. Jia, R.A. Williams, *Particle deposition and aggregation*, Butterworth-Heinemann, 1998, pp. 9-32.

[24] M. Kaisti, Q. Zhang and K. Levon, ”Compact model and design considerations of an ion-sensitive floating gate FET”, Sensors and Actuators B: Chemical, vol. 241, pp. 321-326, 2017.

[25] K. Jayant, K. Auluck, M. Funke, S. Anwar, J.B. Phelps, P.H. Gordon, S.R. Rajwade and E.C. Kan, ”Programmable ion-sensitive transistor interfaces. I. Electrochemical gating”, Physical Review E - Statistical, Nonlinear, and Soft Matter Physics, vol. 88, no. 1, pp. 1-13, 2013

[26] D. Neamen, *Semiconductor physics and devices.* New York, N.Y: McGraw-Hill, 2012.

[27] A. Vladimirescu and S. Liu, ”The simulation of MOS integrated circuits using SPICE2”, University of California at Berkeley, Department of Electrical Engineering and Computer Sciences, Berkeley, CA, 94720, 1980.

[28] T. Ning, P. Cook, R. Dennard, C. Osburn, S. Schuster and H. Yu, ”1 μm MOSFET VLSI technology: Part IV—Hot-electron design constraints”, IEEE Transactions on Electron Devices, vol. 26, no. 4, pp. 346-353, 1979. Available: 10.1109/t-ed.1979.19433.

[29] M. Lenzlinger and E. Snow, ”Fowler-Nordheim Tunneling into Thermally Grown SiO2”, Journal of Applied Physics, vol. 40, no. 1, pp. 278-283, 1969. Available: 10.1063/1.1657043.

[30] J. Ranuárez, M. Deen and C. Chen ”A review of gate tunneling current in MOS devices”, Microelectronics Reliability, vol. 46, no. 12, pp. 1939-1956, 2006. Available: 10.1016/j.microrel.2005.12.006.

[31] Su-Hsia Lin, Chwei-Huann Chiou, Chih-Kai Chang, Ruey-Shin Juang, ”Photocatalytic degradation of phenol on different phases of TiO_2 particles in aqueous suspensions under UV irradiation”, Journal of Environmental Management, vol. 92, no. 12, pp. 3098-3104, 2011.

Appendices

Appendix A

Collaboration

Based on the project proposal, the work was divided in three groups. Most of the work was done within the individual sub-groups. However, in order to prevent overlapping work by the groups, a top-level overview of both the development version and the final version of the system was made.
Due to the circumstance of the COVID-19 crisis, the development of prototypes was prohibited from all BAP projects. The main consequence for us (subgroup C) was that the application part of the project was pushed in a more theoretically detailed direction. This means that the focus was more on the sensor theory and possible sensor enhancements, and less on developing an actual product. As a result, the necessary communication with the other subgroups (within the bounds of the project collaboration) was probably less than it would have been otherwise.
The main communication platform for day-to-day communication with both the group and the supervisors was a Discord server. This platform provides both text channels and voice channels, but is limited in its capability for face-to-face communication. The advantages of using a Discord server as the main communication platform are firstly that it is very easy to join a conversation in either a voice channel or a text channel. Secondly, it is very easy to read back any conversation. The main drawback is the lack of face-to-face communication, which was limited to the main presentations in this project.

Appendix B

Derivations

B.1 Compact modelling procedures

B.1.1 The transconductance, k

The transconductance k can be determined with two approaches;

1st approach

The first one makes use of the previously used $\sqrt{I_D}$ vs V_{GS} plot, from which we can compute the slope. To do this we start with Equation B.1 and take the square root of it, B.2. If then V_T is assumed constant, the equation can be differentiated with respect to V_{GS} to arrive at Equation B.3. All that is left now is to take a small V_{DS} - again, a V_{DS} of $50\ mV$ is significant enough - to disregard channel-length modulation $(1 + \lambda * V_{DS} \cong 1)$ and to rewrite Equation B.3, giving us the desired result of Equation B.4.

$$I_D = \frac{k_n}{2}(V_{GS} - V_T)^2(1 + \lambda V_{DS}) \tag{B.1}$$

$$\sqrt{I_D} = \sqrt{\frac{k_n}{2}(1 + \lambda V_{DS})}(V_{GS} - V_T) \tag{B.2}$$

$$\frac{\partial \sqrt{I_D}}{\partial V_{GS}} = \sqrt{\frac{k_n}{2}(1 + \lambda V_{DS})} \tag{B.3}$$

$$k_n = 2\frac{\partial \sqrt{I_D}}{\partial V_{GS}}^2 \text{ for } \lambda V_{DS} << 1 \tag{B.4}$$

2nd approach

The second approach utilizes a I_D vs V_{DS} plot at $V_{DS} = 0$. k can be determined by taking the slope again, but this time around the transistor is in linear region due to V_{DS} being lower than $V_{GS} - V_T$. So Equation B.5 has to be used, starting off by differentiating it with respect to V_{DS} to get Equation B.6. After that $V_{DS} = 0$ is filled in and the equation is rewritten to the requested form of Equation B.7.

$$I_D = k_n((V_{GS} - V_T)V_{DS} - (\frac{V_{DS}}{2})^2) \tag{B.5}$$

$$\frac{\partial I_D}{\partial V_{DS}} = k_n((V_{GS} - V_T) - V_{DS}) \tag{B.6}$$

$$k_n = \frac{\partial I_D}{\partial V_{DS}}\frac{1}{V_{GS} - V_T} \text{ for } V_{DS} \rightarrow 0 \tag{B.7}$$

The values of k vary significantly between the approaches, because the surface scattering effect is not modeled in the Unified Model. k depends on the vertical field strength through the mobility which in itself depends on V_{GS}. It is however modelled in the Level 2 SPICE model.

B.1.2 The threshold voltage, V_{T0}

The threshold voltage can be estimated by extrapolating the $\sqrt{I_D}$ vs V_{GS} plot to the x-intercept. This is done by equating $\sqrt{I_D}$ to 0 in Equation B.2, resulting in Equation B.8, which can be further simplified to Equation B.9. Note that the maximum V_{GS} for which $\sqrt{I_D}$ is zero needs to be taken. While doing this, V_{DS} needs to be as low as possible to neglect the drain-induced barrier lowering (DIBL) effect, as using a higher V_{DS} will produce a lower V_{T0}.

$$\sqrt{\frac{k_n}{2}(1+\lambda V_{DS})}(V_{GS}-V_T)=0 \tag{B.8}$$

$$(V_{GS}-V_T)=0 \tag{B.9}$$

B.1.3 channel-length modulation, λ

The channel-length modulation factor λ can be determined by linearly extrapolating the current in the saturation region to the left until it hits the x-intercept, i.e., calculating the tangent of the saturation current and solving that linear equation for $y = 0$ giving you a Early voltage V_E situated on the negative x-axis. Next, V_E is entered in equation B.11, which is derived from Equation B.10, with $I_D = 0$ (B.12). Doing this for multiple fixed V_{GS}'s and taking the average gives a more accurate result.

$$I_D = I'_D(1+\lambda V_{DS}) \tag{B.10}$$

$$\lambda = (\frac{I_D}{I'_D}-1)\cdot\frac{1}{V_{DS}}) \tag{B.11}$$

$$\lambda = \frac{-1}{V_E}\text{ for } I_D = 0 \tag{B.12}$$

B.1.4 The saturation voltage, V_{DSAT}

At last the saturation drain voltage V_{DSAT} will be determined. This however can not be easily derived mathematically, so a visual estimation from the I_D vs V_{DS} plot is used. One can either try and spot the transition from the linear region to the velocity-saturation region or fit it on the unified model.

B.1.5 LEVEL 3 extraction methods

Refer to Section 4.10.1 till 4.10.5 of the report of Vladimirescu for extraction procedures of parameters θ, η, δ, V_{max} and κ [27].

Appendix C

ADS

C.1 FGFET parameter extraction schematic

This schematic combines the MOSFET model of Section 3.3 with the floating gate extension as described in Section 3.2. It also incorporates the interconnect resistances. Furthermore a symbol was created so that it could easily be incorporated into other designs. The ADS implementation is as follows and can be seen in Figure C.2; When the optimization button is pressed the nominal optimization component together with a goal is initiated. Important settings are the optimization type, maximum iterations, expression and limit. Hybrid optimization was chosen as it combines the strengths of the Random and Quasi-Newton search methods by finding minima quickly and by being able to find the global cost minimum in the neighbourhood of multiple local minima. The maximum iterations can be chosen arbitrarily large, if time isn't of the essence. For the expression the absolute error was taken with an upper bound of 1e-7 as limit. Similarly, the absolute error of the derivatives was taken. Next a parameter sweep is commenced, sweeping V_{GS} from 1 to 5. Meanwhile, a file index variable depending on V_{GS} selects the appropriate measurement file from the data file list component, which where split into separate files for each V_{GS} beforehand. In the process of sweeping V_{GS} it will do a DC sweep of V_{DS}. Apart from being used in the circuit, V_{DS} also influences the data index of the measurement file. The data was converted beforehand to the MDIF discrete data format. Conjointly, a third goal is optimized which is a copy of the first goal except it now DC sweeps V_{GS} from 0 to 5, but this can also be split into two separate circuits. The optimization parameters can be bounded or unconstrained, the option is found under 'Simulation -> Simulation Variables Setup -> Optimization'.

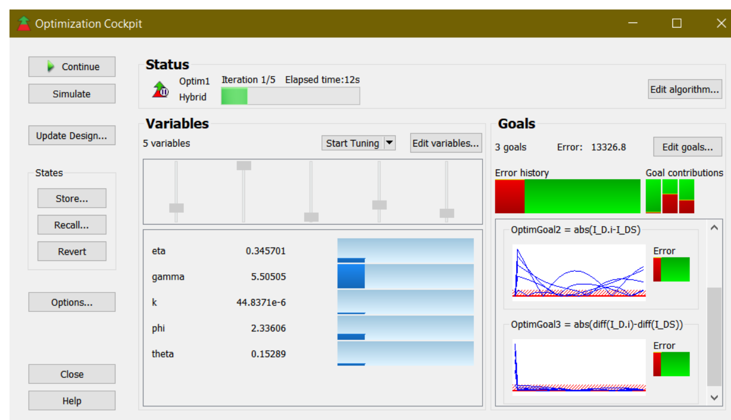

Figure C.1: A view of the optimization cockpit running the ADS implementation of FGFET parameter extraction.

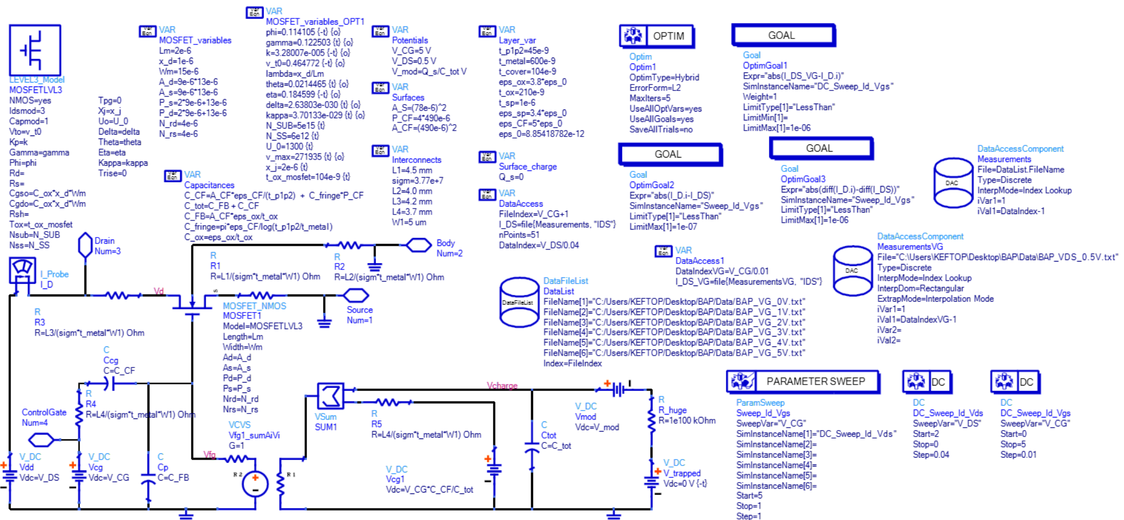

Figure C.2: The ADS implementation of FGFET parameter extraction using the optimizer

C.2 ISFGFET with sensing area model

TODO

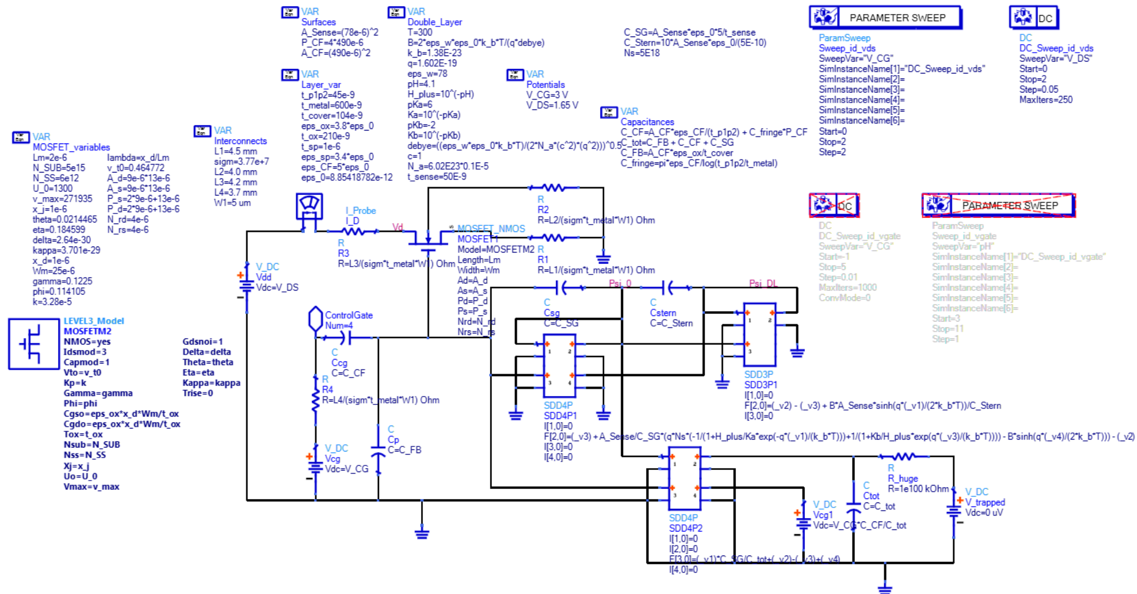

Figure C.3: The ADS implementation of ISFGFET simulation, extended to include the double layer model.

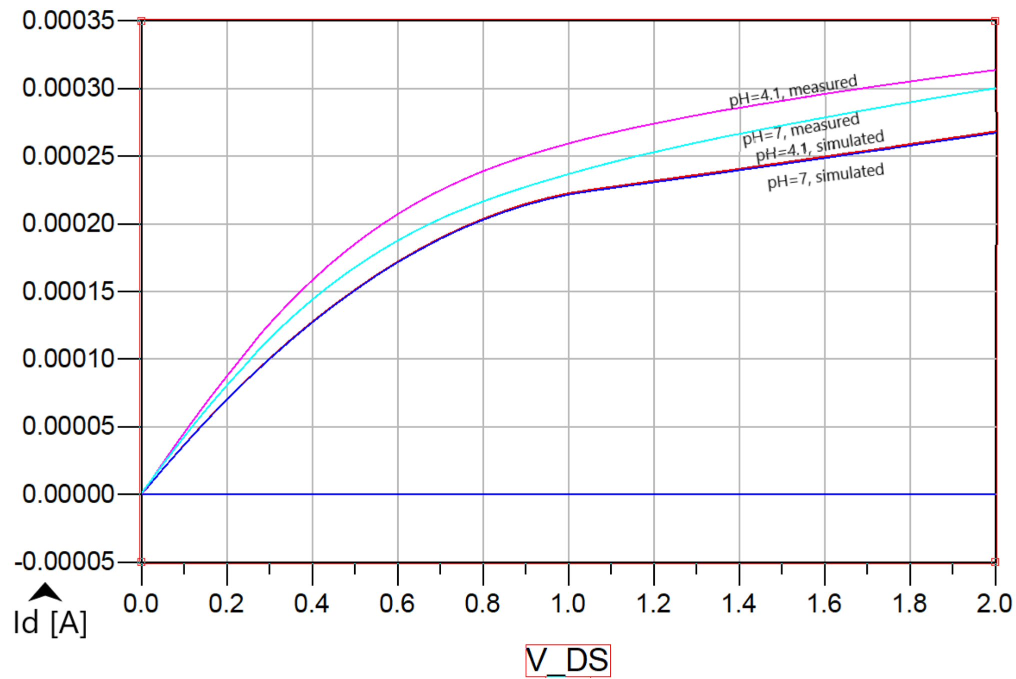

(a)

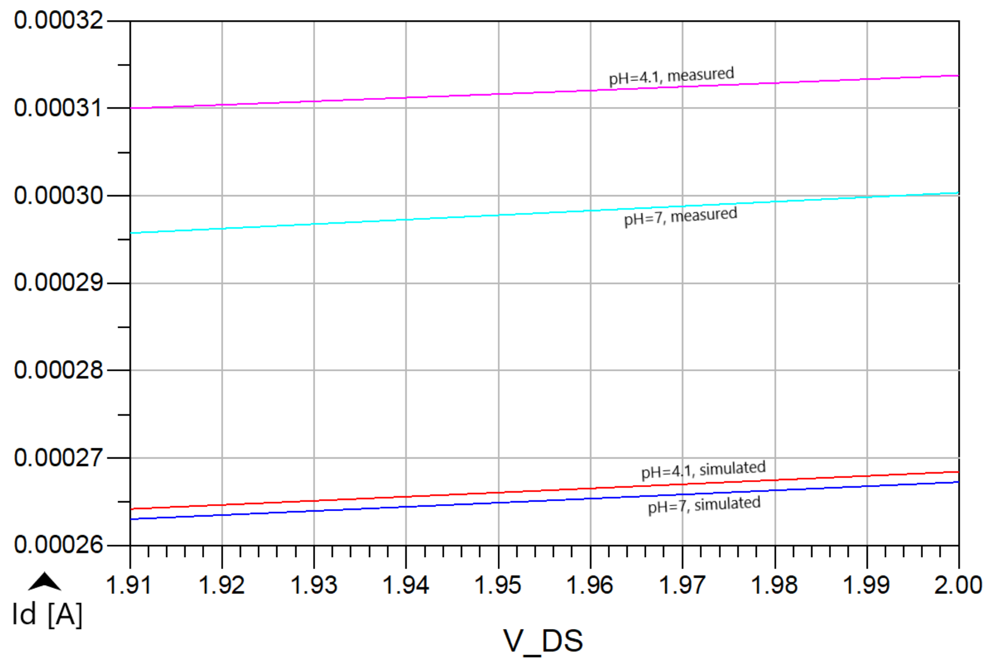

(b)

Figure C.4: (a) Simulated and measured response of the ISFGFET to a solution bulk pH different for $V_{CG} = 2V$. (b) Zoomed in pH response.

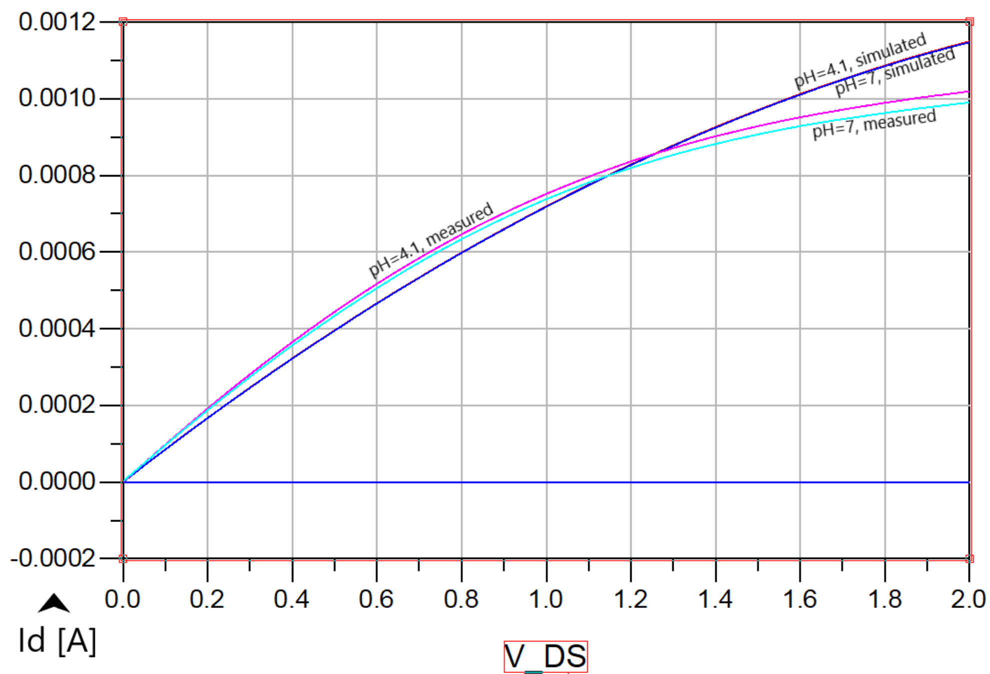

(a)

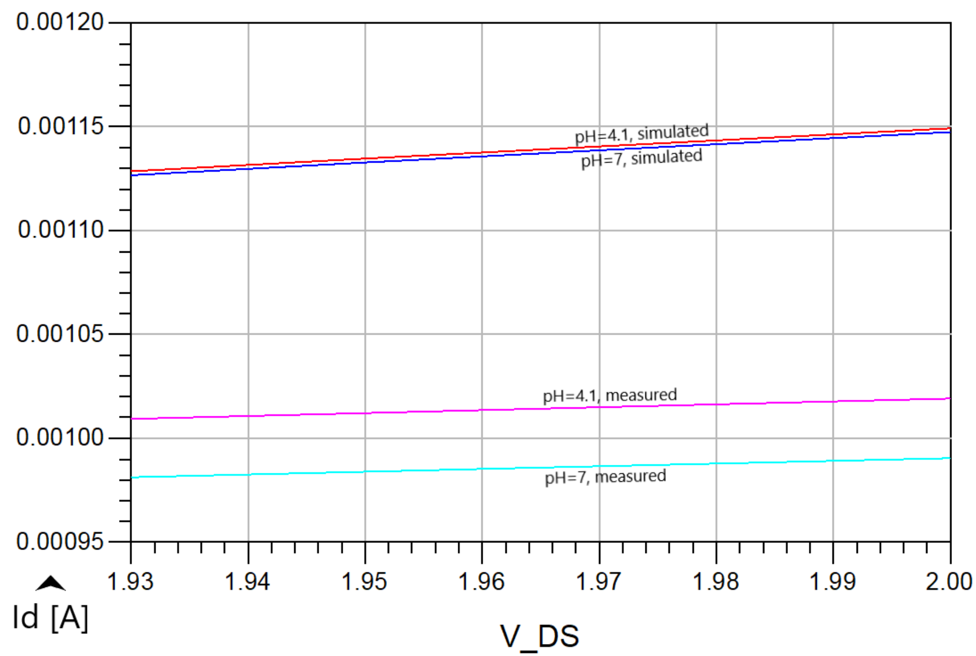

(b)

Figure C.5: (a) Simulated and measured response of the ISFGFET to a solution bulk pH different for $V_{CG} = 2V$. (b) Zoomed in pH response.

Appendix D

MATLAB simulation

D.1 EDL

```
breaklines
%Sensor dimensions:
t_CF = 45E-9;               %Control gate capacitor dielectric thickness
t_metal = 600E-9;           %Floating gate Al thickness
t_ox_undoped = 104E-9;      %Oxide thickness over undoped areas
t_ox_doped = 210E-9;        %Oxide thickness over NW, SN and SP doped areas

eps_0 = 8.85418782E-12;     %Vacuum permittivity
eps_ox = 3.8*eps_0;         %Oxide permittivity
eps_CF = 5*eps_0;           %Control gate capacitor dielectric permittivity

A_CF = (490E-6)^2;          %Control gate capacitor mutual area
P_CF = 4*sqrt(A_CF);        %Control gate capacitor perimeter

%Capacitances:
C_CF = A_CF*eps_CF/t_CF + pi*eps_CF/log(t_CF/t_metal);
C_FB = A_CF*eps_ox/t_ox_undoped;

%MOSFET parameters
L_m = 2E-6;         %Channel length
W_m = 15E-6;        %Channel width
V_t0 = 0.43;        %Threshold voltage
x_d = 1E-6;
lambda = x_d/L_m;   %Channel length modulation
mu_n = 0.1350;      %Carrier mobility
theta = 0.1529;     %Mobility attenuation
c_i = eps_ox/t_ox_doped;    %Oxide capacitance per unit area
C_ox = c_i*W_m*L_m;         %Mosfet oxide capacitance

%Sensing Area: parameters
A_s = (78E-6)^2;                        %Sensing pad surface area
t_ox_SG = 0.1*20E-9;                        %Sensing pad oxide thickness
C_SG = A_s*eps_ox/t_ox_SG;              %Sensing pad oxide capacitance
C_Stern = A_s*10*eps_0*0.01/(5E-10);    %Stern capacitance
C_tot = C_CF+C_FB+C_SG;

Ns =8E18;           %Total fixed number of binding sites per unit area
k = 1.3806E-23;     %Boltzmann constant
T = 293;            %Temperature
```

```
39 z = 1;                %Ion charge number
40 eps_w = 78;           %Relative permittivity of water
41 q = 1.602E-19;        %Elementatry charge
42
43 %Sensing Area: Solution parameters
44 N_a = 6.02E23*5E-5;           %Ion concentration
45 debye = sqrt(eps_w*eps_0*k*T/(2*N_a*z^2*q^2));  %Debye length
46 B = 2*eps_w*eps_0*k*T/(q*debye);
47
48 %Bias point
49 V_DS = 3;        %Drain-source voltage
50 Q_0 = 0;         %Floating gate trapped charge
51
52 steps = 5;
53 pHsteps = 21;
54 V_CG = 3.3;
55
56 %intitialize solution matrices
57 val_E_ox = zeros(steps, pHsteps);
58 val_V_FG = zeros(steps, pHsteps);
59 val_Psi_0 = zeros(steps, pHsteps);
60 val_Psi_DL = zeros(steps, pHsteps);
61 val_sigm_0 = zeros(steps, pHsteps);
62 val_sigm_DL = zeros(steps, pHsteps);
63
64 I_D0 = zeros(steps, pHsteps);
65 pH = zeros(0,pHsteps);
66
67 %Double layer model definition
68 syms V_FG Psi_0 Psi_DL sigm_0 sigm_DL
69
70 for pHstep = 1:21
71 pH(pHstep) = 0.5 + 0.5*pHstep;
72 H_plus = 10^(-pH(pHstep));  %H-plus bulk concentration
73
74 for i = 1:steps
75
76     pK_A = 6;            %-log10(K_A)
77     pK_B = -4 +(i-1)*4;           %-log10(K_B)
78     K_A = 10^(-pK_A);    %Dissociation constant A
79     K_B = 10^(-pK_B);    %Dissociation constant B
80
81     %System of equations
82     eqn1 = V_FG == C_CF*V_CG/C_tot + (Q_0)/C_tot + C_SG*Psi_DL/C_tot;
83     eqn2 = Psi_0 == V_FG + A_s*(sigm_0 + sigm_DL)/C_SG;
84     eqn3 = Psi_DL == Psi_0 + A_s*sigm_DL/C_Stern;
85     eqn4 = sigm_0 == -q*Ns/(1+(H_plus/K_A)*exp(-q*Psi_0/(k*T))) ...
86         + q*Ns/(1+(K_B/H_plus)*exp(q*Psi_0/(k*T)));
87     eqn5 = sigm_DL == -B*sinh(q*Psi_DL/(2*k*T));
88     eqns = [eqn1, eqn2, eqn3, eqn4, eqn5];
89
90     %Equation solver
91     S = vpasolve(eqns, [V_FG, Psi_0, Psi_DL, sigm_0, sigm_DL]);
92
93     %fill in solver value
94     val_V_FG(i, pHstep) = double(S.V_FG);
95     val_Psi_0(i, pHstep) = double(S.Psi_0);
96     val_Psi_DL(i, pHstep) = double(S.Psi_DL);
```

```
97      val_sigm_0(i, pHstep) = double(S.sigm_0);
98      val_sigm_DL(i, pHstep) = double(S.sigm_DL);
99
100     %electric field in the oxide
101     val_E_ox(i, pHstep) = (val_V_FG(i)-val_Psi_0(i))/t_ox_SG;
102
103     %Effective carrier mobility
104     mu_eff = mu_n/(1+theta*(val_V_FG(i, pHstep)-V_t0));
105     %Saturation drain-source voltage
106     V_DSsat = V_DS - V_t0;
107
108     alpha = mu_eff*c_i*W_m/(2*L_m)*(1+lambda*(V_DS-V_DSsat));
109     %Saturation region drain current
110     I_D0(i, pHstep) = alpha*(val_V_FG(i,pHstep)-V_t0)^2;
111
112 end
113
114 end
115
116 plot(pH, val_V_FG)
117 xlabel('pH')
118 ylabel('Floating gate voltage [V]')
119 legend('pKb=-4', 'pKb=0', 'pKb=4', 'pKb=8', 'pKb=12')
```

D.2 Fowler-Nordheim tunneling estimation

```
breaklines
1  %FN tunneling
2
3  close all;
4  A = 0.5e-6*3.75e-6;      % area (m^2)
5  t = 10e-9;               % oxide thickness (m)
6  %A = 2e-6*15e-6;         % area (m^2)
7  %t = 45e-9;              % oxide thickness (m)
8  q = 1.6e-19;             % electronic charge (C)
9  h = 6.62607015e-34;      % planck constant (Js)
10 hb = 1.054571817e-34;    % reduced planck constant (Js)
11 m = 0.26*9.11e-31;       % free-electron mass (kg) for condictivity
12 p = 2.7*1.6e-19;         % barrier height (J)
13 V = 0:0.1:20;            % Gate Voltage
14 unit = 1e12;             % pA
15
16 I = A*q^3.*V.^2 ./( 8*pi*h*p*t^(2) ) .* ...
17     exp(-4*sqrt(2*m)*p^(3/2)*t ./(3*hb*q.*V) )*unit;
18
19 figure;
20 semilogy(V,I,'lineWidth',1.5);
21 text()
22 ylim([1e-20 1e-11]*unit)
23 ylabel('I (pA)')
24 xlabel('V_{CG} (V)')
25 %title({'Fowler-Nordheim tunneling current as a', ...
26 %              ' function of the control gate voltage'})
27 grid on
28 current_ax = gca; % get the current axis;
29 % set the width of the axis (the third value in Position)
30 % to be 60% of the Figure's width
```

```
31 current_ax.Position(3) = 0.6;
32 % put the textbox at 75% of the width and
33 % 10% of the height of the figure
34 str = {"$A \ = \ $" + A,"$t_{ox} \ = \ $" + t,"$q \ = \ $" + q, ...
35     "$h \ = \ $" + h,"$\hbar \ = \ $" + hb,"$m \ = \ $" + m, ...
36     "$\Phi \ = \ $" + p};
37 anno = annotation('textbox',[0.15, 0.55, 0.3, 0.3],'interpreter','latex',...
38     'String', str,'FitBoxToText','on');
39 anno.EdgeColor = 'white';
40
41 %apply style sheet info
42 % load('style.mat')
43 % fnam='myfig.eps'; % your file name
44 % s.Format = 'eps'; %I needed this to make it work but maybe you wont.
45 % hgexport(gcf,fnam,s);
```